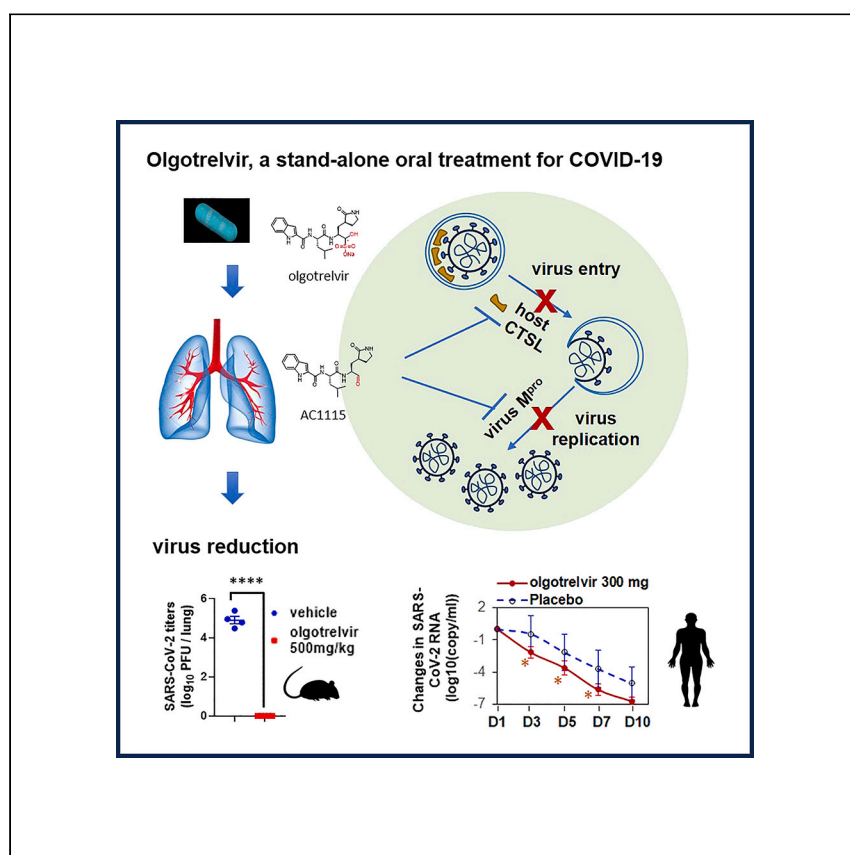


Clinical and Translational Article

Olgotrelvir, a dual inhibitor of SARS-CoV-2 M^{pro} and cathepsin L, as a standalone antiviral oral intervention candidate for COVID-19

Mao et al. discovered and developed a next-generation antiviral, olgotrelvir, as a standalone treatment for COVID-19 without ritonavir. Olgotrelvir, with a dual mechanism of action targeting SARS-CoV-2 M^{pro} and human cathepsin L, significantly inhibited virus replication in an animal model and in COVID-19 patients by oral administration.

Long Mao, Namir Shaabani, Xiaoying Zhang, ..., Henry Ji, Hongzhou Lu, Xiao Xu

luhongzhou@fudan.edu.cn (H.L.)
xxu@aceatherapeutics.com (X.X.)

Highlights

Olgotrelvir can be administered orally as a standalone treatment without ritonavir

Olgotrelvir targets SARS-CoV-2 M^{pro} and host cathepsin L

Both virus entry and virus replication are blocked in the infected cells

Virus replication is inhibited in an animal model and in COVID-19 patients



Mao et al., Med 5, 42–61
January 12, 2024 © 2023 The Authors.
Published by Elsevier Inc.
<https://doi.org/10.1016/j.medj.2023.12.004>



Clinical and Translational Article

Olgotrelvir, a dual inhibitor of SARS-CoV-2 M^{pro} and cathepsin L, as a standalone antiviral oral intervention candidate for COVID-19

Long Mao,¹ Namir Shaabani,² Xiaoying Zhang,³ Can Jin,¹ Wanhong Xu,³ Christopher Argent,⁴ Yulia Kushnareva,¹ Colin Powers,² Karen Stegman,² Jia Liu,¹ Hui Xie,² Changxu Xu,³ Yimei Bao,³ Lijun Xu,³ Yuren Zhang,³ Haigang Yang,³ Shengdian Qian,³ Yong Hu,³ Jianping Shao,³ Can Zhang,³ Tingting Li,³ Yi Li,³ Na Liu,³ Zhenhao Lin,³ Shanbo Wang,³ Chao Wang,³ Wei Shen,³ Yuanlong Lin,⁵ Dan Shu,⁵ Zhenhong Zhu,¹ Olivia Kotoi,¹ Lisa Kerwin,² Qing Han,⁶ Ludmila Chumakova,¹ John Teijaro,⁷ Mike Royal,² Mark Brunswick,² Robert Allen,^{2,8} Henry Ji,² Hongzhou Lu,^{5,*} and Xiao Xu^{1,9,*}

SUMMARY

Background: Oral antiviral drugs with improved antiviral potency and safety are needed to address current challenges in clinical practice for treatment of COVID-19, including the risks of rebound, drug-drug interactions, and emerging resistance.

Methods: Olgotrelvir (STI-1558) is designed as a next-generation antiviral targeting the SARS-CoV-2 main protease (M^{pro}), an essential enzyme for SARS-CoV-2 replication, and human cathepsin L (CTSL), a key enzyme for SARS-CoV-2 entry into host cells.

Findings: Olgotrelvir is a highly bioavailable oral prodrug that is converted in plasma to its active form, AC1115. The dual mechanism of action of olgotrelvir and AC1115 was confirmed by enzyme activity inhibition assays and co-crystal structures of AC1115 with SARS-CoV-2 M^{pro} and human CTSL. AC1115 displayed antiviral activity by inhibiting replication of all tested SARS-CoV-2 variants in cell culture systems. Olgotrelvir also inhibited viral entry into cells using SARS-CoV-2 Spike-mediated pseudotypes by inhibition of host CTSL. In the K18-hACE2 transgenic mouse model of SARS-CoV-2-mediated disease, olgotrelvir significantly reduced the virus load in the lungs, prevented body weight loss, and reduced cytokine release and lung pathologies. Olgotrelvir demonstrated potent activity against the nirmatrelvir-resistant M^{pro} E166 mutants. Olgotrelvir showed enhanced oral bioavailability in animal models and in humans with significant plasma exposure without ritonavir. In phase I studies (ClinicalTrials.gov: NCT05364840 and NCT05523739), olgotrelvir demonstrated a favorable safety profile and antiviral activity.

Conclusions: Olgotrelvir is an oral inhibitor targeting M^{pro} and CTSL with high antiviral activity and plasma exposure and is a standalone treatment candidate for COVID-19.

Funding: Funded by Sorrento Therapeutics.

INTRODUCTION

Severe acute respiratory syndrome coronavirus 2 (SARS-CoV-2) is an RNA virus that has caused a 3-year-long pandemic with millions of deaths across the globe. Despite the unprecedented speed of development and approval of SARS-CoV-2 vaccines and treatments, there remain large swaths of un-vaccinated populations

CONTEXT AND SIGNIFICANCE

Human society is still vulnerable to COVID-19 post pandemic due to constantly emerging new variants of concern, especially patients at risk. Oral drugs with broad-spectrum antiviral activity and limited potential drug-drug interaction risks are urgently needed. Researchers at ACEA Therapeutics discovered and developed a next-generation antiviral, olgotrelvir, that demonstrated potent inhibition of both virus entry and virus replication in infected cells by targeting M^{pro} and cathepsin L. The dual mechanism of action significantly increased its antiviral activity in cells and in an animal model. Researchers also demonstrated that olgotrelvir can be used safely as a standalone treatment for COVID-19 without ritonavir as a booster in healthy volunteers and COVID-19 patients, which reduces the risk of drug-drug interactions.

and an increasing incidence of breakthrough cases due to low antibody titers and infection by new variants of concern (VOCs) that have continued to plague the world. With the current prevailing Omicron variants, protection from the original vaccines and repeated boosters with modified vaccines has been limited due to rapidly disappearing immunity.^{1,2} Continued development of safe and effective SARS-CoV-2 antivirals with durable activity against emerging VOCs will provide a necessary complement to vaccine therapies, particularly in immunocompromised populations.

Orally administered SARS-CoV-2 antivirals are attractive candidates to fill this persistent public health need. SARS-CoV-2 replication requires non-structural proteins cleaved from the 2 nascent polyproteins encoded by the virus genome.³ Of the 14 cleavage sites in the 2 polyproteins, three sites are cut by papain-like protease, while the remaining sites are processed by the main protease (M^{PRO}).³ SARS-CoV-2 M^{PRO} is highly conserved in betacoronaviruses, including all SARS-CoV-2 variants, with C145 as a catalytic residue.^{4,5} Given that there are no M^{PRO} homologs in humans, M^{PRO} is an ideal target for anti-SARS-CoV-2 drugs against a broad spectrum of variants.^{4,6} Currently, a SARS-CoV-2 M^{PRO} inhibitor, nirmatrelvir, has emergency use authorization (EUA) for coronavirus disease 2019 (COVID-19) treatment as an oral pill (<https://www.fda.gov/drugs/emergency-preparedness-drugs/coronavirus-covid-19-drugs>). Nirmatrelvir (co-administered with ritonavir) can be used for early-stage patients with mild symptoms who are at high risk for disease progression. Treatment with nirmatrelvir requires co-administration of ritonavir (RTV), a strong cytochrome P450 (CYP450) 3A4 inhibitor and pharmacokinetic boosting agent,⁷ which introduces the attendant risk of otherwise avoidable drug-drug interactions (DDIs) and limits broad use of nirmatrelvir (<https://www.pfizer.com/products/product-detail/paxlovidtm>). The risk of serious side effects or complications due to DDI-related medication adjustments increases the healthcare burden in the context of COVID treatment. In addition, virus resistance to first-line antiviral therapies is an ongoing concern because strains harboring mutations on M^{PRO} that abolish the nirmatrelvir inhibitory activity were isolated from patients treated with nirmatrelvir. Although there is no report indicating potential dominance of such mutant strains and related failure of nirmatrelvir treatment in clinical practices, the development of compounds with diverse mechanisms of action could increase the barrier to emergence of resistant variants.^{8–10}

Initiation of the virus replication cycle requires SARS-CoV-2 entry into host cells and subsequent redirection of host translation machinery to synthesize virus-encoded proteins. Upon binding to host cell ACE2 receptors, Spike proteins are cleaved to expose the S2 subunit, which mediates virus membrane fusion and subsequent release of virus RNA into the host cytosol.⁵ There are two viral entry pathways: one mediated by the host serine protease TMPRSS2 for cell surface fusion and a second mediated by the host lysosomal cysteine protease cathepsin L (CTSL) for endosomal entry and fusion (reviewed by Liu et al.¹¹). SARS-CoV-2 utilizes both entry pathways, with a reported preference for utilization of the TMPRSS2 pathway by earlier SARS-CoV-2 VOCs and a preference for CTSL mediated endosomal pathway by the more recently prevalent Omicron VOCs.^{12–14} Although the expression level of both TMPRSS2 and CTSL in tissues may affect the preference of the Omicron VOC entry pathway,^{15,16} further data from primary cell cultures and from *in vivo* models is required to definitively corroborate these findings. Still, inhibitors of host proteases, in particular CTSL, have been explored as anti-SARS-CoV-2 compounds.¹⁷ Clinically approved drugs with CTSL inhibition activities also displayed certain anti-viral activities against coronaviruses, including SARS-CoV-2, SARS-CoV, and

¹ACEA Therapeutics, Inc., San Diego, CA 92121, USA

²Sorrento Therapeutics, Inc., San Diego, CA 92121, USA

³ACEA Pharmaceutical Co., Ltd., Hangzhou, Zhejiang, P.R. China

⁴Scientia Clinical Research Limited, Sydney, NSW, Australia

⁵Shenzhen Third People's Hospital, SUSTech, Shenzhen, P.R. China

⁶Structure Based Design, Inc., San Diego, CA 92121, USA

⁷Department of Immunology and Microbial Science, The Scripps Research Institute, La Jolla, CA 92037, USA

⁸Present address: Invivyd, Inc., Waltham, MA 02451, USA

⁹Lead contact

*Correspondence:
luhongzhou@fudan.edu.cn (H.L.),
xxu@aceatherapeutics.com (X.X.)

<https://doi.org/10.1016/j.medj.2023.12.004>

MERS-CoV.¹¹ Additionally, a few small molecules with inhibition activity against both SARS-CoV-2-encoded enzymes and CTSL showed anti-viral activities in cell culture or animal models.^{18,19}

Olgotrelvir is a novel, orally administered prodrug optimized from a collection of compounds designed to inhibit SARS-CoV-2 M^{Pro} by covalently binding to Cys145. Olgotrelvir and its parent drug AC1115 displayed potent antiviral activities against SARS-CoV-2 variants in cell culture models and in humanized transgenic mouse models of SARS-CoV-2 pathogenesis. In addition, olgotrelvir inhibits the activity of human CTSL, the major cysteine protease aiding virus entry through the endosomal pathway utilized by the prevalent Omicron variants.^{12–14} The dual inhibition of both virus entry and downstream virus replication pathways may enhance the robustness of the antiviral effect and reduce potential drug resistance. Pharmacokinetics (PK) studies demonstrated that olgotrelvir has excellent oral bioavailability and limited DDIs, allowing it to be used as a standalone treatment without the need for co-administration of CYP inhibitors or P-glycoprotein inhibitors. Considering the favorable efficacy and PK profile along with data supporting the positive safety profile of the compound, olgotrelvir is a promising second-generation anti-SARS-CoV-2 drug candidate that warrants further development as a next-generation therapeutic intervention for COVID-19 and other coronaviruses.

RESULTS

Medicinal chemistry and structure biology

Our design of SARS-CoV-2 M^{Pro} inhibitors was based on the reported crystal structures of SARS-CoV-2 M^{Pro}^{20,21} with a focus on potent inhibition of M^{Pro} and on antiviral activities, favorable oral bioavailability, and safety profiles with good solubility and chemical stability. A variety of warhead groups on several scaffolds were evaluated for dual inhibition activities of both SARS-CoV-2 M^{Pro} and human CTSL, in addition to the compounds' metabolic stability and oral PK properties. After several rounds of structural modifications, olgotrelvir (molecular weight [MW] = 516.5) as a prodrug was selected from a group of advanced lead compounds and nominated as a clinical candidate. An efficient synthetic route was developed with a seven-step synthesis, as described in [STAR Methods](#). Because olgotrelvir is readily converted to its active form, AC1115 (MW = 412.5), in biorelevant media and human blood, both olgotrelvir and AC1115 were evaluated in different *in vitro* studies.

To gain insight into the dual mechanisms of SARS-CoV-2 inhibition for this chemical series, high-resolution co-crystal structures of AC1115 with SARS-CoV-2 M^{Pro} and human CTSL were determined at 1.8 Å and 1.4 Å, respectively. The co-crystal structure of SARS-CoV-2 M^{Pro} in complex with AC1115 illustrates a covalent linkage between the aldehyde warhead and the sulfur atom of C145 at the M^{Pro} catalytic active site ([Figure 1](#)), which is 100% conserved in all SARS-CoV-2 variants.⁵ AC1115 fits well in the catalytic active-site pocket, forming multiple favorable hydrophobic and hydrophilic interactions with M^{Pro} ([Figures 1B and 1C](#)). The P1-lactam of the compound occupies the S1 site of M^{Pro} and forms hydrogen bonds with the side chains of E166 and H163 as well as the backbone of L141. The P3-leucine side chain of the compound fits in the S2 pocket of the protein, making favorable contacts within the cleft of the active site ([Data S1](#)). The compound is capped with an indole ring that contacts M^{Pro} across a flexible loop composed of residues 189–192. A total of 7 hydrogen bonds are observed between the compound and the protein, with additional water-mediated hydrogen bonds also evident ([Figure 1C](#)).

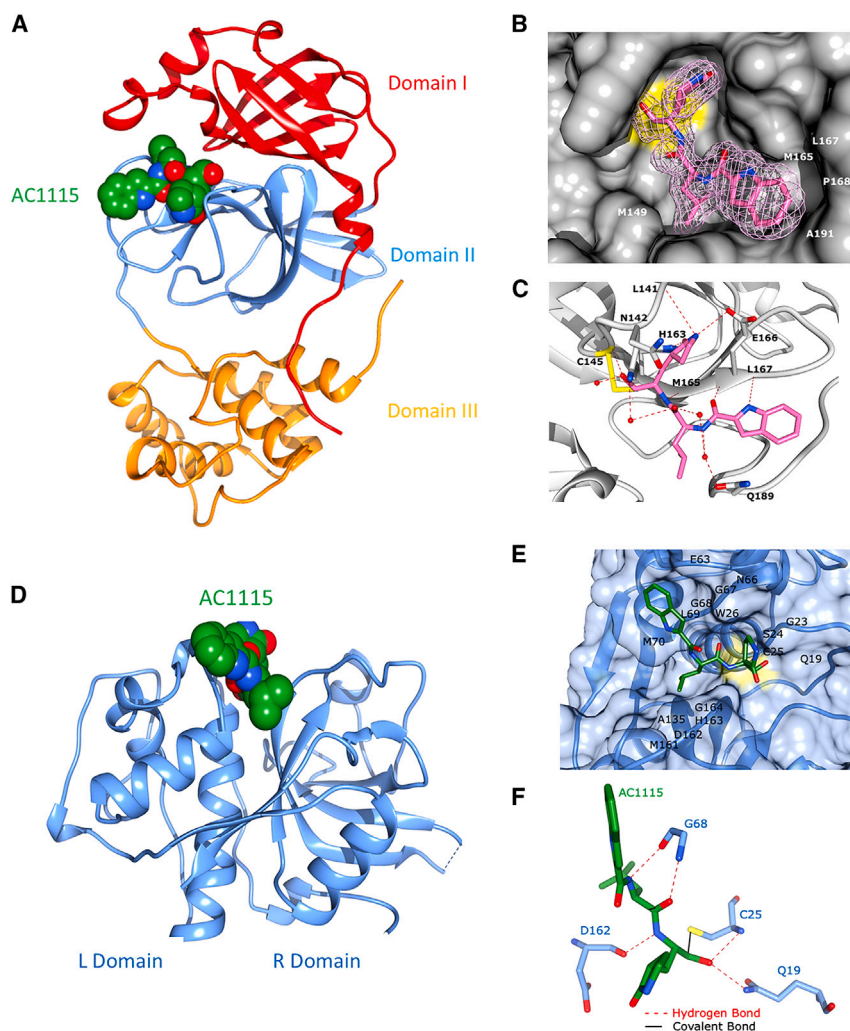


Figure 1. High-resolution co-crystal structure of SARS-CoV-2 M^{Pro} or human CTSL complexed with AC1115

(A–C) Co-crystal structure of SARS-CoV-2 M^{Pro} complexed with AC1115.

(A) SARS-CoV-2 M^{Pro} is shown in ribbon representation, with domains I, II, and III labeled. The inhibitor AC1115 is represented as spheres.

(B) SARS-CoV-2 M^{Pro} (gray surface) bound with compound (pink sticks). Electron density corresponding to the compound is shown as pink mesh. Hydrophobic residues of the M^{Pro} catalytic active-site binding pocket are labeled, with the active-site cysteine shown in yellow.

(C) Hydrogen bond interactions between the compound and M^{Pro} are denoted with black lines. The compound forms 7 direct hydrogen bonds with M^{Pro} residues, with additional polar interactions mediated by water molecules (red spheres).

(D–F) Co-crystal structure of human CTSL complexed with AC1115.

(D) CTSL (blue) is shown in ribbon representation, with the L and R domains labeled. The inhibitor AC1115 is depicted as spheres.

(E) CTSL protein (surface and cartoon) with covalently bound AC1115 (green sticks). Amino acid residues contacting AC1115 are labeled; the catalytic cysteine (C25) is additionally indicated by the yellow protein surface.

(F) AC1115 hydrogen bonds with CTSL amino acids are shown (red dashed lines), along with the covalent bond to the C25 side-chain sulfur atom (black line).

These figures and the protein structure figures in the supplements of this paper were prepared using Chimera.²²

The co-crystal structures of CTSL complexed with AC1115 revealed a covalent linkage between the aldehyde warhead and the sulfur atom of the C25 at the CTSL catalytic active site (Figures 1E and 1F). AC1115 fits well in the active-site pocket, forming favorable hydrophobic and hydrophilic interactions with CTSL (Data S2). Although the P1-lactam and the indole ring of AC1115 do not form hydrogen bonds with CTSL, the backbone of AC1115 forms one hydrogen bond with D162 and two hydrogen bonds with G68 (Figures 1E and 1F). In addition to forming a covalent bond with C25, the oxygen of the warhead group of AC1115 forms one hydrogen bond with the side chain of C25 and the side chain of Q19, respectively. A total of 5 hydrogen bonds are observed between AC1115 and CTSL, with additional water-mediated hydrogen bonds also apparent (Figure 1F).

Dual inhibition of M^{Pro} and CTSL and *in vitro* antiviral activities

The dual inhibitory activities of AC1115 were tested in enzymatic assays. AC1115 displayed potent inhibition of both wild-type M^{Pro} from the WA-1 strain and Omicron M^{Pro}, which harbors a P132H change (<https://www.ncbi.nlm.nih.gov/activ>), with IC₅₀ (half maximal inhibitory concentration) values of 2.44 and 14.27 nM, respectively (Figure 2A). The respective inhibitory potencies are similar to those of nirmatrelvir.^{23,24} The inhibition was reversible; more than 70% of the M^{Pro} activity was recovered within 5 min after an equimolar ratio of inhibitor/enzyme mixture was diluted 100 × in reaction buffer (Figure 2B). AC1115 also displayed potent reversible inhibition of human CTSL activity, with an IC₅₀ value around 0.06 nM (Figure 2D). Several other members of the human cysteine cathepsin family were also tested for inhibition by AC1115, with IC₅₀ values in the nanomolar range, more than 40 times higher than those recorded in assays with CTSL (Data S3). Furthermore, AC1115 was tested against a panel of 56 human and virus proteases. Other than the cysteine cathepsins and β-CoV M^{Pro}, AC1115 showed no significant inhibition against other proteases (Data S4). The *in vitro* enzyme activity inhibition data are consistent with the covalent interactions illustrated in the co-crystallization structure of AC1115 complexed with the active sites of SARS-CoV-2 M^{Pro} and human CTSL (Figure 1).

The antiviral activities of olgotrelvir and its *in vivo* active form AC1115 were evaluated *in vitro* using different types of cell systems. In Vero E6 cells, using a plaque reduction neutralization test (PRNT), olgotrelvir and AC1115 displayed antiviral activity against all tested SARS-CoV-2 VOCs, including WA-1, Alpha, Beta, Delta, Lambda, and Gamma variants. The average EC₅₀ (half maximal effective concentration) values were between 0.28 and 4.26 μM, similar to those of nirmatrelvir (Data S5). No evidence of cytotoxicity was observed under the same compound treatment conditions, including when cells were incubated with up to 100 μM olgotrelvir or AC1115 (Data S6). Using a focus reduction neutralization test (FRNT), which enables detection of Omicron variant replications, similar antiviral potency as in the PRNT was observed for olgotrelvir and AC1115 against WA-1 (Figure 2C; Data S7A and S7B). Both AC1115 and olgotrelvir displayed potent antiviral activity against WA-1 and Omicron BA.5 (Figure 2C). It is worth noting that, compared with nirmatrelvir, the antiviral activities of olgotrelvir and AC1115 were relatively independent of p-glycoprotein inhibitors such as CP-100356, indicating favorable absorption of these compounds into cells and an overall metabolic stability consistent with use of AC1115 as a standalone therapeutic drug (Data S7A). Olgotrelvir antiviral effects were also verified in the EpiAirway system composed of differentiated normal human bronchial epithelial cells (dNHBE), with an antiviral EC₅₀ value below 41 nM (Data S7C), which was in the same EC₅₀ range as for nirmatrelvir.²³ Again, no significant cytotoxicity was observed with up to 100 μM olgotrelvir under the assay conditions (Data S6).

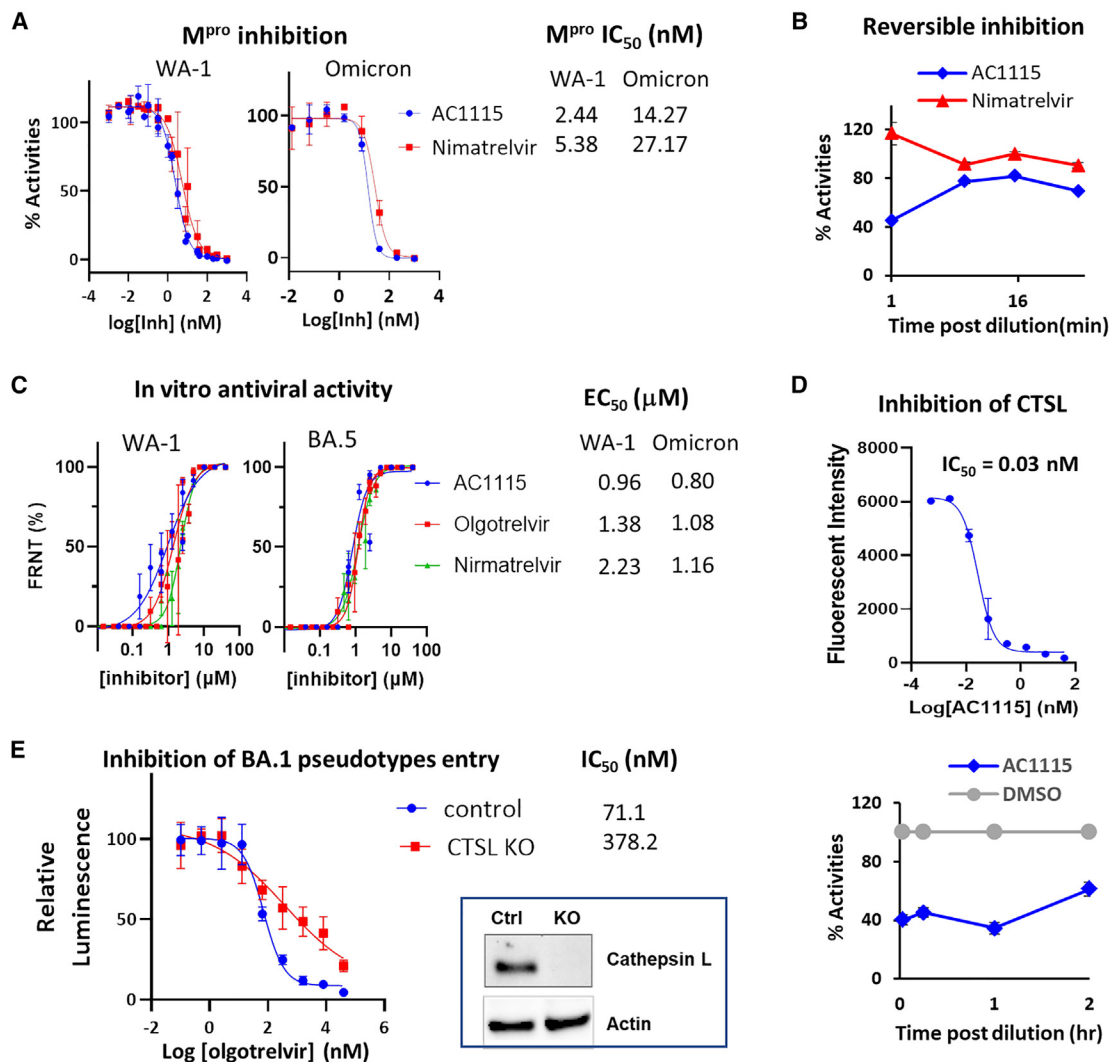


Figure 2. Olgotrelvir and AC1115 in vitro activities

(A) AC1115 potently inhibits recombinant SARS-CoV-2 M^{pro}. Enzyme concentrations used in the assays were 17 nM and 34 nM for WA-1 and Omicron M^{pro}, respectively. WA-1 results are the average and standard deviations from 4 independent experiments with duplicates for each experiment. For Omicron M^{pro}, representative data with duplicates for each data point are shown.

(B) AC1115 reversibly inhibits SARS-CoV-2 M^{pro}. 3.4 μM recombinant SARS-CoV-2 WA-1 M^{pro} was incubated with 3.4 μM AC1115 or nirmatrelvir for 30 min before 1:100 dilution in assay buffer. M^{pro} activity was determined at 1 min, 5 min, 15 min, and 60 min post dilution. Activity is calculated as the initial rates of the reaction and expressed as percentage of control values in DMSO-treated samples. Shown are representative data with average and standard deviation of duplicates for each data point.

(C) Olgotrelvir antiviral effect against SARS-CoV-2 WA-1 and Omicron BA.5 in Vero E6 cells. 1,000 plaque-forming units (PFUs) of SARS-CoV-2 variants were used for infection for the shown experiment. Each data point on the plot was the average and standard deviation of 8–10 data points from 2–3 independent experiments with 2–4 replicates for each experiment.

(D) AC1115 inhibits recombinant human CTSL activity (top), and the inhibition is reversible (bottom). Equimolar amounts of CTSL and AC1115 were incubated for 30 min before 1:100 dilution in the reaction buffer. CTSL activities were determined at the indicated time points. Shown are representative results with average and standard deviation of duplicates for each data point.

(E) Olgotrelvir inhibits SARS-CoV-2 BA.1 Spike-mediated pseudotype entry. CTSL KO was verified by western blot analysis. To compare inhibition of pseudotype entry in different cells, luminescence is normalized to cells transduced with pseudotype without compound treatment. Shown is a representative result with average and standard deviation of quadruplicates for each data point.

To explore whether olgotrelvir and AC1115 deter viral entry into host cells by inhibition of the cathepsin-dependent endosomal pathway, SARS-CoV-2 S protein pseudotyped recombinant vesicular stomatitis virus (rVSV)-ΔG-luciferase was used in pseudovirus entry assays. In HEK Blue hACE2 TMPRSS2 cells, both the cathepsin

pathway and the TMPRSS2 pathway can mediate pseudovirus entry. Olgotrelvir displayed similar inhibition properties as the pan-cathepsin inhibitor E-64D, with about 60% entry inhibited for Omicron (BA.1 and BA.4/5) Spike pseudotypes and about 30% entry inhibited for D614G (WA-1) or Delta Spike pseudotypes (Data S8A and S8B). On the contrary, the TMPRSS2 inhibitor camostat had greater inhibition of D614G and Delta Spike pseudotypes than of Omicron Spike pseudotypes. These data are consistent with reports indicating that Omicron favors the cathepsin entry pathway, while most other SARS-CoV-2 variants favor the TMPRSS2 entry pathway.^{12–14} Nirmatrelvir showed no inhibition activity in any of the pseudotype entry assays, consistent with a report showing that it has no inhibitory activity of human cathepsins²³ (Data S8A). To further confirm olgotrelvir inhibition of CTSL-dependent virus entry, we generated HEK Blue-hACE2-TMPRSS2 CTSL knockout (KO) cells, which eliminate CTSL-mediated entry but preserve the TMPRSS2 pathway for virus entry (Figure 2E). As expected, this led to decreased pseudovirus entry in KO cells compared with that observed in parental cells (Data S8D). The inhibition potency of olgotrelvir on pseudotypes entry in these CTSL KO cells was decreased for the 2 tested pseudoviruses, including D614G and BA.1, with IC₅₀ values for BA.1 Spike pseudotypes increased to 378.2 nM from 71.1 nM in parental cells (Figure 2E and Data S8E). In HEK Blue hACE2 cells, in which only the endosomal cathepsin pathway is prevalent, olgotrelvir at 10 μM exhibited nearly complete inhibition of entry of each pseudovirus tested, including those mediated by Spike proteins from D614G, Delta, and Omicron BA.1 and BA.4/5 (Data S8B). The IC₅₀ values were between 54.52 and 81.35 nM (Data S8C). These results strongly suggest that olgotrelvir antiviral activity can be achieved through engagement of dual targets: inhibition of viral replication by targeting SARS-CoV-2 M^{Pro} and blockade of virus entry by targeting host CTSL.

Inhibition of M^{Pro} mutants of concern

Since the first report of COVID-19, thousands of SARS-CoV-2 variants have been reported. M^{Pro} mutations have been found in 3 major VOCs (Lambda, Beta, and Omicron). Olgotrelvir and AC1115 inhibited activities of all of these mutant M^{Pro}s (Data S9), which is consistent with the antiviral activity of olgotrelvir on these VOCs (Figure 2C; Data S5 and S7A). To further evaluate potential drug resistance, 13 additional M^{Pro} mutations identified in nirmatrelvir-treated patient or cell culture samples^{24,25} were selected and generated as recombinant proteins. Inhibition potencies on the mutant enzyme activities were determined for olgotrelvir, AC1115, and nirmatrelvir. Some of these mutations, such as E166V and H172Y, displayed resistance to nirmatrelvir inhibition.^{9,25–28} Olgotrelvir displayed inhibitory activity against all of these mutants with similar to significantly higher potency than nirmatrelvir (Data S9). Notably, for two mutants containing E166V mutations, nirmatrelvir was ineffective, while olgotrelvir showed inhibitory activity with IC₅₀ values in the low nanomolar range: 57.8 and 18.6 nM for the E166V mutant and the E166V/L55F double mutations, respectively (Data S9).

Further context for the *in vitro* inhibition data may be gained from the co-crystal structures of SARS-CoV-2 M^{Pro} in complex with AC1115. Three hydrogen bonds were formed between E166 and AC1115 (Data S1C), while the nirmatrelvir molecule could form only two hydrogen bonds with E166. The additional hydrogen bond was contributed from the indole ring of AC1115 (the unique structure of olgotrelvir/AC1115), while the *t*-butyl group at the same position of nirmatrelvir did not establish an evident hydrogen bond with E166.²⁹ This difference in overall M^{Pro} E166 binding characteristics between AC1115 and nirmatrelvir may contribute to the observed differences between olgotrelvir/AC1115 and nirmatrelvir inhibitory

activities against the E166 mutants. Other mutations, such as K90R and P132H, which were found in the M^{PfO} of B.1.351 (Beta) and B.1.1.529 (Omicron), respectively, are far from the ligand binding sites based on the co-crystal structure. Accordingly, these mutations have no significant impact on olgotrelvir or nirmatrelvir inhibitory activities against the two respective M^{PfO} variants.

In vitro cytotoxicity and safety profiling

AC1115, the active form of olgotrelvir, displayed little cytotoxicity at concentrations up to 100 μ M under varied culture conditions (e.g., stationary and log phase) in cell lines derived from important organs/tissues (Data S6 and S10A). In addition, potential mitochondrial toxicity of AC1115 was evaluated in cells grown in galactose medium, and no differences in cytotoxicity for cells grown in glucose vs. galactose medium were observed (Data S10B).

We further tested AC1115 against the SAFETYscan47 KdMAX Panel (Eurofins/DiscoverX) to evaluate potential undesirable pharmacodynamic effects in humans. At 100 μ M, AC1115 did not display significant activity on any of the tested targets (Data S11). These results projected a strong preclinical safety profile for olgotrelvir; its *in vivo* active form, AC1115, displayed no detectable toxicity in *in vitro* evaluations of the molecule.

In vivo antiviral activity and reduction of lung pathology in a mouse model

In vivo antiviral activity of olgotrelvir was tested in K18-hACE2 transgenic mice, which express human ACE2 in the lung epithelia, including airway epithelia, under the control of the human keratin 18 promoter. After intranasal infection with the SARS-CoV-2 WA-1 strain, mouse body weight loss was approximately 20% on day 5 post infection, indicating severe disease progression (Figure 3A). Such body weight loss was fully prevented by oral administration of olgotrelvir twice a day (BID) at a dosage of 500 or 1,000 mg/kg immediately after viral inoculation (Figure 3A). On day 5 post infection, virus was below the detectable level in the lungs, as determined either by the viral plaque assay using lung homogenates or by immunohistochemistry assay detecting viral nucleocapsid protein (NP) staining in mouse lung slices (Figures 3B and 3D, top). Correspondingly, pathological changes caused by SARS-CoV-2 infection were relieved, with significantly lower pathology scores recorded in the lung tissues in the treatment group than in the vehicle group (Figures 3C and 3D, bottom). Notably, in a therapeutic model, olgotrelvir at a dose of 1,000 mg BID administered orally at the 12th hour post-infection resulted in significant reduction of viral RNA shedding (approximately 2 log) and prevention of the body weight loss, indicating strong *in vivo* antiviral activity (Figures 3E and 3F).

Olgotrelvir's effect on the production of pro-inflammatory cytokines (interleukin-6 [IL-6], tumor necrosis factor alpha [TNF- α], and granulocyte-macrophage colony-stimulating factor [GM-CSF]) induced by SARS-CoV-2 was tested in the lungs of K18-hACE2 transgenic mice following oral administration of 400 mg/kg BID. Olgotrelvir administered on this regimen prevented mice from weight loss caused by SARS-CoV-2 infection and blocked pro-inflammatory cytokine release (Data S12) compared with animals in the control treatment group.

PK and toxicological profiles in animals

The pharmacology properties and safety profiles of olgotrelvir and the active form AC1115 were evaluated in *in vitro* cell models and *in vivo* animal models as well as in healthy human volunteer subjects. AC1115 was stable in plasma of various species and showed much lower clearance rates in human liver microsomes and human

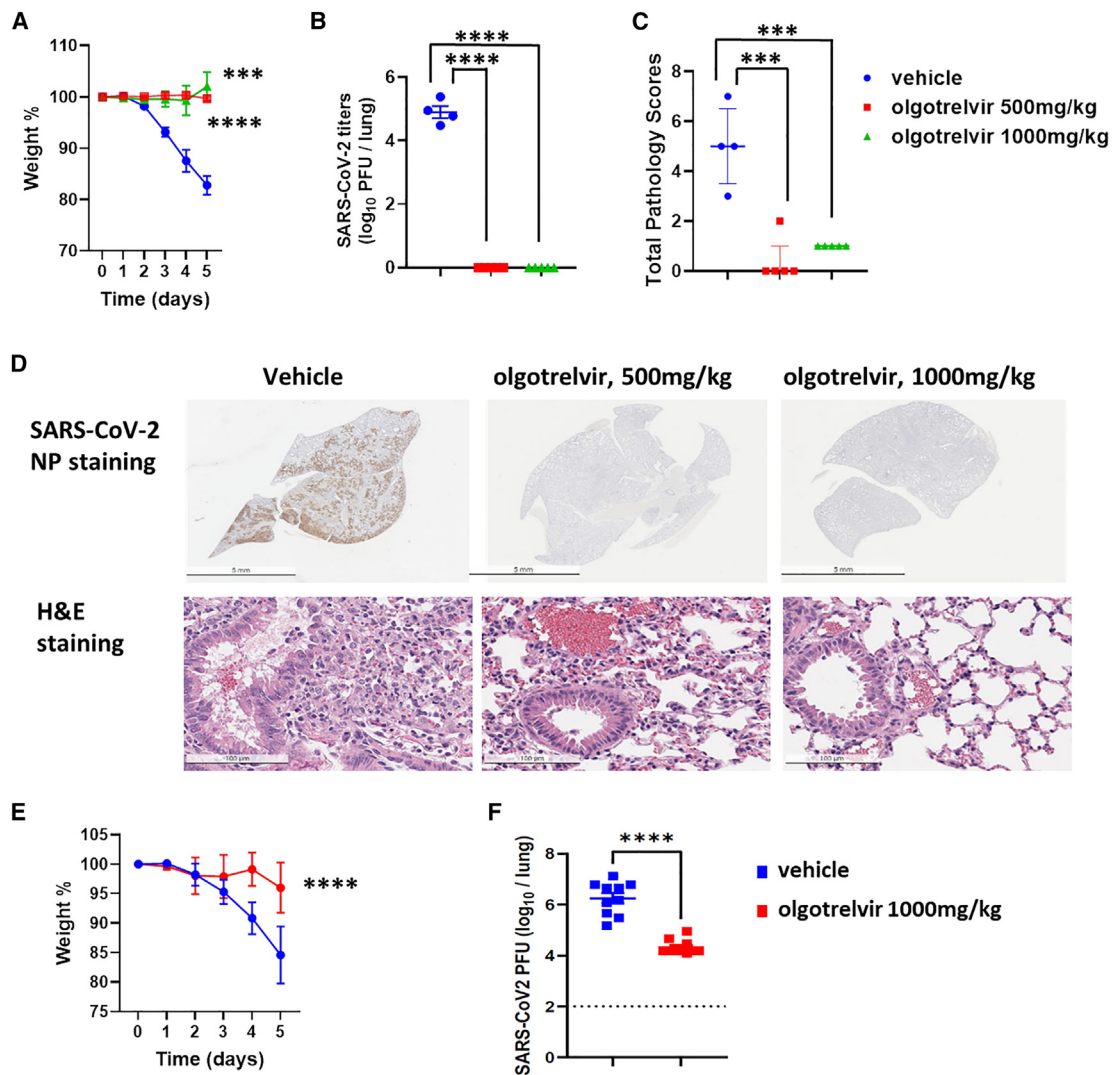


Figure 3. Olgotrelvir in vivo antiviral effect

K18-hACE2 transgenic mice were intranasally infected with 5,000 PFUs of SARS-CoV-2 WA-1 and treated orally with olgotrelvir BID for 5 days. Mice were weighed daily before being sacrificed for analysis.

(A–D) Immediately following virus infection, mice were treated with olgotrelvir BID at the indicated doses.

(A) Olgotrelvir prevented mouse weight loss associated with SARS-CoV-2 infection. Shown are the average and standard deviation of each group of 5 mice.

(B) Olgotrelvir cleared SARS-CoV-2 from infected mouse lungs. Virus loads were determined by PRNT in Vero E6 cells.

(C) Olgotrelvir reduced lung pathology caused by SARS-CoV-2 infection. Shown are pathology scores obtained from hematoxylin and eosin (H&E)-stained mouse lung slices. A 5-point scoring system with scores of 0–4 was applied, with 4 indicating most severe damage for the following parameters: perivascular inflammation, bronchial or bronchiolar epithelial degeneration or necrosis, bronchial or bronchiolar inflammation, and alveolar inflammation. The overall pathology score was the sum of the scores for the 4 categories.

(D) Representative images of immunohistochemistry (IHC) and H&E-stained mouse lung slices. Top: IHC staining with anti-SARS-CoV-2 NP for visualizing virus load. Bottom: H&E staining for pathology evaluation.

(E and F) 12 h post SARS-CoV-2 infection, mice were treated with 1,000 mg/kg/day olgotrelvir BID. (E) Olgotrelvir prevented weight loss. Shown are average and standard deviation of each group of 10 mice. (F) Olgotrelvir cleared SARS-CoV-2 from infected mouse lungs.

: 0.0001 < p < 0.001; *: p < 0.0001.

hepatocytes (half-life [$t_{1/2}$], 78.7 min; intrinsic clearance [CL_{int}], 11.0 mL/min/kg; extraction ratio [ER], 0.34) than nirmatrelvir ($t_{1/2}$, 21.1 min; CL_{int} , 41.2 mL/min/kg; ER, 0.66) at the same test concentration of 0.2 μ M, indicating good human liver microsome stability of olgotrelvir (Table 1).

Table 1. Liver microsomal stability of olgotrelvir

Compound	Test species	$t_{1/2}$ (min)	CL_{int} (mL/min/kg)	ER
Olgotrelvir	human	78.7	11.0	0.34
	beagle dog	276.0	6.3	0.15
	Sprague-Dawley rat	31.7	39.2	0.47
	CD-1 mouse	72.8	37.5	0.46
Nirmatrelvir	human	21.1	41.2	0.66
	beagle dog	155.0	11.1	0.24
	Sprague-Dawley rat	141.0	8.8	0.17
	CD-1 mouse	8.7	314.0	0.88

The metabolic stability of olgotrelvir (0.2 μ M) was evaluated by measurement of AC1115 concentration following incubation with liver microsomes of the indicated species for 60 min at 37°C. Nirmatrelvir without RTV was included as a positive compound. $t_{1/2}$, half-life; CL_{int} , intrinsic clearance; ER, extraction ratio.

To further analyze the role of CYP450 isozymes on the metabolism of AC1115, *in vitro* CYP450 phenotyping studies of AC1115 using either a combination enzyme method (Data S13) or a chemical inhibition method (Data S14) were conducted. The results indicated that CYP3A4 is the primary contributor to the metabolism of AC1115. Seven major CYP450 isozymes were evaluated in human liver microsomes for activity inhibition by AC1115. The results showed that AC1115 had a weak inhibitory effect on CYP2D6 (IC_{50} = 24.33 μ M) (Data S15). In time-dependent inhibition (TDI) CYP isozyme testing, AC1115 only displayed 36.9% inhibition of CYP3A4 activity at 100 μ M (IC_{50} > 100 μ M), using testosterone as a model substrate in human liver microsomes. AC1115 had no inhibitory effect or potential TDI on other enzymes in human liver microsomes at test concentrations up to 100 μ M (Data S16). The data indicate a low risk of CYP inhibition-related DDIs associated with olgotrelvir. By comparison, optimal nirmatrelvir activity by the prescribed regimen is dependent on co-administration of RTV, which is known to be a strong CYP3A4 inhibitor.⁷ Additionally, AC1115 was studied as a potential substrate or inhibitor of human ATP-binding cassette (ABC) transporters. AC1115 was not a substrate of either breast cancer resistance protein (BCRP) or MDR1 transporters at any of the tested concentrations up to 50 μ M, indicating a low DDI risk with BCRP or MDR1 inducers/inhibitors in humans (Data S17). Neither olgotrelvir nor AC1115 at concentrations up to 50 μ M demonstrated inhibition potential on MDR1, and a weak inhibition potential on BCRP with the IC_{50} value of 18.9 and 27.8 μ M, respectively, was observed (Data S18).

Plasma exposure of AC1115 was analyzed in mouse, rat, dog, and monkey by oral administration of olgotrelvir (Table 2). AC1115 exhibited moderate to low plasma clearance, moderate steady-state volume of distribution (V_{ss}), and longer plasma $t_{1/2}$ in non-rodents than in rodents. As a result, the oral bioavailability of olgotrelvir in dogs and monkeys was 84.7% and 48.3%, respectively, much higher than in rodents (Table 2). In a mouse model, co-administration of RTV did not increase the plasma exposure or other PK parameters of AC1115 (Data S19), indicating that olgotrelvir metabolic stability is independent of RTV in mice. To study tissue penetration of AC1115 in the lungs, the exposure of AC1115 in rat lung tissue was analyzed in comparison with the plasma exposure after orally administered olgotrelvir. AC1115 reached peak concentration in the lungs 30 min post administration and remained in the lung tissue for more than 12 h, with a concentration in the lungs over 7-folds higher than the plasma concentration (Data S20).

Olgotrelvir was tolerable in animal toxicology studies, as shown in Data S21. A set of systematic toxicology studies was conducted to evaluate the safety of olgotrelvir.

Table 2. PK parameters of AC1115 after a single dose with AC1115 (i.v.) or olgotrelvir (po) in animals

Species	Dose (mg/kg)	AUC _{inf} (ng h/mL)	t _{1/2} (h)	C _{max} (ng/mL)	T _{max} (h)	F (%)
Mouse	10 (i.v.)	5,290	3.45	–	–	–
	300 (po)	8,030	1.58	7,290	0.25	5.06
	500 (po)	12,400	1.90	10,600	0.25	4.69
	1,000	28,600	1.47	16,300	0.25	5.41
Rat	5 (i.v.)	3,410 ± 425	3.19 ± 1.46	–	–	–
	100 (po)	2,000 ± 938	1.48 ± 0.0549	1,200 ± 555	0.17 (0.083–0.025)	2.94 ± 1.37
	200 (po)	3,580 ± 1,910	1.84 ± 0.302	2,650 ± 1,580	0.083 (0.083–0.083)	2.62 ± 1.40
	500 (po)	8,050 ± 1.960	2.03 ± 0.516	6,460 ± 2,930	0.083 (0.083–0.25)	2.36 ± 0.57
Dog	2 (i.v.)	2,920 ± 548	13.3 ± 1.83	–	–	–
	12.5 (po)	15,200 ± 3.840	4.01 ± 0.438	3,600 ± 998	2.0 (1.0–2.0)	83.1 ± 21.0
	25 (po)	30,500 ± 13,600	3.76 ± 0.579	7,080 ± 1,900	1.5 (0.25–2.0)	83.5 ± 37.4
	50 (po)	61,800 ± 17,400	3.51 ± 0.310	13,200 ± 3,220	2.0 (0.5–3.0)	84.7 ± 23.9
Monkey	2.5 (i.v.)	5,600 ± 2,030	8.57 ± 0.44	10,100 ± 2,530	–	–
	84 (po)	90,900 ± 21,100	4.84 ± 0.41	18,800 ± 4,690	2.7 (2.0–4.0)	48.3 ± 11.3

Olgotrelvir, a prodrug, was readily converted to its active form, AC1115, in full blood and/or plasma. Therefore, after oral administration of olgotrelvir in the fed state or intravenous (i.v.) administration of AC1115 to different species, AC1115 was quantified in plasma with EDTA-K2 as anticoagulant using liquid chromatography-tandem mass spectrometry (LC-MS/MS) assays. Gender difference was generally not observed in nonclinical species. Data are presented as mixed genders as mean values (± standard deviation where applicable). AUC_{inf}, area under the concentration-time curve from time 0 extrapolated to infinity; t_{1/2}, half-life; C_{max}, maximum plasma concentration; T_{max}, time to maximum plasma concentration, expressed as median (range); CL, total plasma clearance; V_{ss}, steady-state volume of distribution; F (%), oral bioavailability.

Generally, no functional changes in vital organs or systems were identified. In the general toxicological studies, rats could tolerate olgotrelvir with dose levels up to 2,000 mg/kg/day for 14 consecutive days with minimal/mild and reversible microscopic changes in the thyroid, stomach, and pancreas, which were considered non-adverse effects with relatively low risk in humans. For beagle dogs, the maximum tolerated dose (MTD) of a single oral dose of olgotrelvir was judged to be greater than 1,000 mg/kg. In the 14-day dog repeat dose toxicity study, loose/watery feces, emesis, and salivation at dose levels from 150–400 mg/kg/day were the symptoms observed during the dosing period, and such clinical signs were reversed during recovery period. In a standard battery of genotoxicity studies, olgotrelvir and/or AC1115 was determined to be neither mutagenic nor clastogenic.

PK, safety, and antiviral activity in humans

A phase I study has been conducted in healthy volunteers (ClinicalTrials.gov: NCT05364840) to evaluate the safety and PK of olgotrelvir as a standalone treatment. This is a 2-part, randomized, double-blind, placebo-controlled, single ascending dose (SAD; part 1) and multiple ascending dose (MAD; part 2) study. A total of 58 volunteers participated either in the olgotrelvir or placebo group. The first subject was enrolled and treated on June 2, 2022. As shown in Figure 4A, after a single oral administration of olgotrelvir capsules under the fasting condition, olgotrelvir was rapidly absorbed with the median time to maximum plasma concentration (T_{max}) of AC1115 ranging from 0.5–1.5 h. The terminal t_{1/2} was in the range of 21.1–26.0 h. The plasma exposure of AC1115 (area under the plasma concentration-time curve from time zero to time of the last quantifiable concentration [AUC_{0-t}], area under the plasma concentration-time curve from time zero to infinity [AUC_{0-inf}] and maximum plasma concentration [C_{max}]) increased proportionally with the increasing doses of olgotrelvir. The mean AUC_{0-inf} was 14,200, 29,200, 43,900 and 94,900 h·ng/mL by a single oral administration of olgotrelvir capsules at 300 mg, 600 mg, 1200 mg and 2,000 mg, respectively. In the MAD portion of the study, the plasma concentration of AC1115 increased along with the increase in doses on both day 1 and day 8. No accumulation was seen on day 8 after 15 consecutive

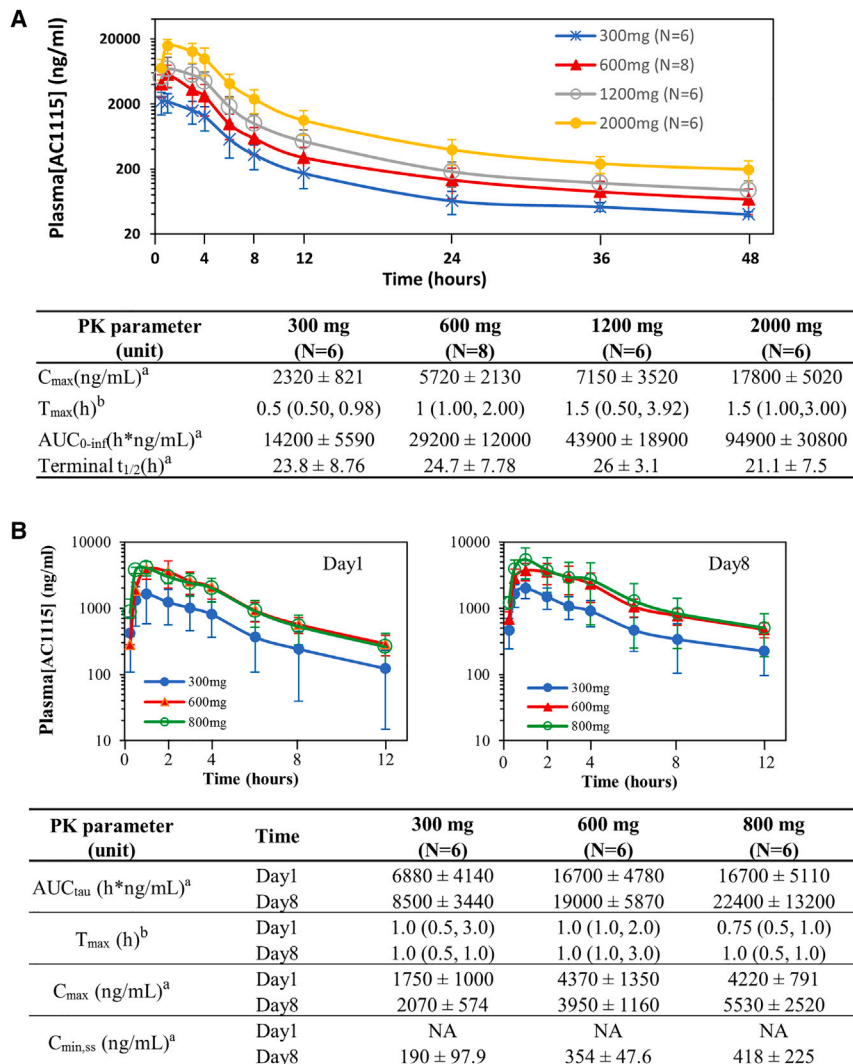


Figure 4. PK of olgotrelvir in healthy human volunteers administered olgotrelvir orally

(A) PK of AC1115 in the SAD portion. Top: Plasma concentration-time plot of AC1115. Healthy human subjects were orally administered a single dose of olgotrelvir under fasting status. N is the number of subjects in each cohort. Presented are plasma concentrations of AC1115 (mean ± standard deviation) at the indicated time points after drug administration. Bottom: summary of plasma PK parameters of AC1115 following SAD.

(B) PK of AC1115 in the MAD portion. Healthy human volunteers were orally administered the indicated dosages BID for 7.5 consecutive days. Top: plasma concentration-time plot of AC1115 on day 1 (first day) and day 8 (last day of olgotrelvir administration). Shown are plasma concentrations of AC1115 (mean ± standard deviation) at the indicated time points after drug administration. N is the number of subjects in each cohort. Bottom: summary of plasma PK parameters of AC1115 following MAD on day 1 and day 8.

AUC_{tau} , area under the plasma concentration-time curve from time 0 to the end of the dosing interval; T_{max} , time to maximum plasma concentration, expressed as median (range); C_{max} , maximum plasma concentration; $C_{min,ss}$, minimum steady-state plasma concentration; NA, not available; BID, twice a day; SAD, single ascending dose; MAD, multiple ascending dose. ^aData are presented as mean ± std. ^bData are presented as median (minimum, maximum).

doses in the 300 mg BID, 600 mg BID, and 800 mg BID cohorts (Figure 4B). In the mouse model, clear antiviral activity can be seen by oral administration of olgotrelvir at the dose of 500 mg/kg (Figure 3) with corresponding daily plasma exposure (AUC) of approximately 24,800 ng·h/mL (Table 2). Therefore, the PK profiles in human healthy volunteers strongly indicate that an efficacious exposure of olgotrelvir could be reached without RTV, supporting olgotrelvir as a standalone treatment for COVID-19.

For safety evaluation, the specific adverse events (AEs) related to the study drug olgotrelvir were summarized and reported by system organ class (SOC) and preferred term (PT) in Data S22 and S23. In the SAD portion of the study, in total, 4 AEs were reported to be drug related by 4 subjects (11.1%), of which 3 AEs were reported by 3 subjects in the olgotrelvir group, and 1 AE was reported by 1 subject in the placebo group (Data S22). In the olgotrelvir group, only headache was considered to be drug related, of which 1 subject (12.5%) was reported in the olgotrelvir (600 mg) group, and 2 subjects (33.3%) reported in the olgotrelvir (1,200 mg) group. In the placebo group, only myalgia, reported by 1 subject (12.5%), was considered to be drug related. In the MAD portion of the study, no drug-related AEs were reported in the placebo group (Data S23). The only drug-related AEs in the olgotrelvir group were ALT and AST elevation in 2 subjects (33.3%) (1 was grade 1 and another was grade 2) in the olgotrelvir (800 mg) group without bilirubin elevation. The alanine transaminase (ALT) and aspartate aminotransferase (AST) elevations occurred transiently late in treatment, did not require discontinuation of the study drug, and resolved over time. It is worth noting that the 800-mg dose is 33% higher and the 7.5 days of treatment are 50% longer than the planned therapeutic dose of 600 mg every 12 h for 5 days. The safety profile suggests olgotrelvir to be advanced in later stage clinical trials.

To explore the antiviral activity of olgotrelvir in COVID-19 patients, a separate phase Ib study was conducted in COVID-19 patients (MPR-COV-101CN; ClinicalTrials.gov: NCT05523739). In this trial, 41 asymptomatic and mild COVID-19 adult patients were treated with 300 mg BID (n = 7), 600 mg BID (n = 16), 800 mg BID (n = 6), and placebo (n = 12) for 7.5 days, and nasal samples were collected on day 1 (pre-treatment), day 3, day 5, day 7, and day 10. Samples were tested for SARS-CoV-2 viral RNA copy numbers by RT-PCR. The viral RNA copy number reduction was measured by comparison with the viral RNA copy numbers on day 1. As shown in Figure 5, patients treated with olgotrelvir demonstrated fast reduction of viral RNA copies compared with placebo control on day 3 (2 days of treatment). Combined with samples from 3 dose groups, the viral RNA copy load was decreased 1.36 log₁₀ (p = 0.019) on day 3, 1.22 log₁₀ (p = 0.048) on day 5, and 1.17 log₁₀ on day 7 (p = 0.01). The antiviral activity in deferent dose cohorts was also analyzed (Figure 5B). Olgotrelvir demonstrated a positive trend of reducing the SARS-CoV-2 viral RNA copy load in each dose group, although the patient numbers for each group were small. The antiviral activity will be further studied in the phase III trial.

DISCUSSION

Paxlovid (nirmatrelvir plus RTV) is the first oral SARS-CoV-2 M^{Pro} inhibitor authorized to treat mild to moderate COVID-19 patients at risk for disease progression. Despite the clinical effectiveness in reducing viral shedding and preventing hospitalization and death,^{30,31} after finishing a course of Paxlovid, about 6%–19% patients get symptom relapse and revert to a virus-positive status within 30 days,^{32,33} and this symptom and virological relapse is now commonly referred to as Paxlovid rebound.

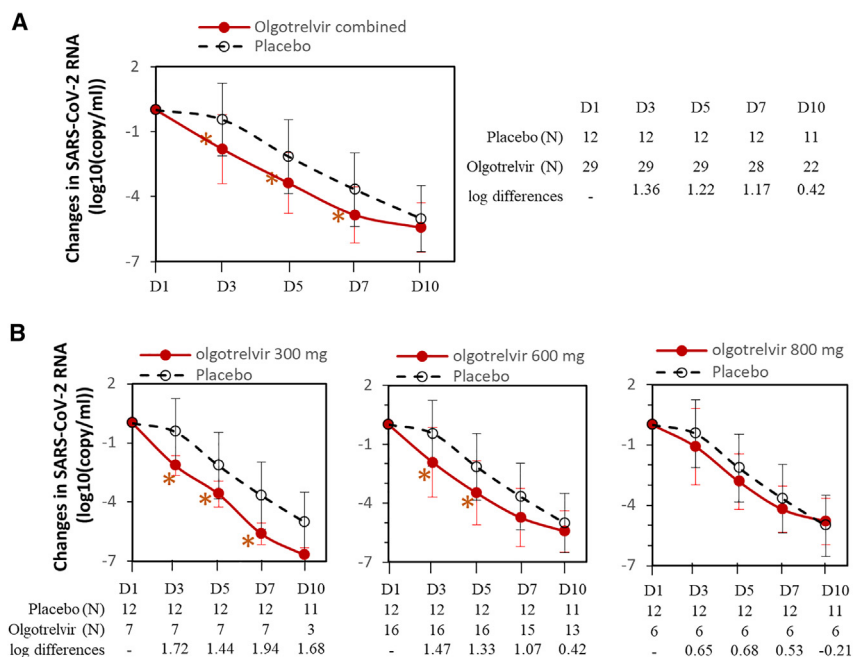


Figure 5. Antiviral efficacy of olgotrelvir

(A) Change from baseline in SARS-CoV-2 RNA levels over time (modified intention-to-treat population) of COVID-19 patients treated with 3 different dosages of olgotrelvir combined compared with placebo. Shown are mean \pm standard deviation. Day 1 to Day 10 refers to the day when samples were collected for analysis. Day 1 is the day when the first sample was collected before the first dose of olgotrelvir given that day. The chart on the right indicates the number of subjects in each cohort at different time points (N), and RNA copy number log reduction differences shown at the bottom of the chart. * $p < 0.05$ based on a t test.

(B) Change from baseline in SARS-CoV-2 RNA copy levels over time (modified intention-to-treat population) of each treatment cohort compared with placebo. Shown are mean \pm standard deviation. RNA copy number log reduction differences are shown at the bottom. * $p < 0.05$ based on a t test.

While the biological underpinning of this phenomenon is still unclear, the rebound has been reported to occur more often in patients with a high viral load.³³ However, rebound symptoms have also been reported in untreated patients,³⁴ and the impact of Paxlovid on the frequency and severity of rebound symptoms remains to be further investigated.³⁵ More potent oral antivirals are needed, and therapies targeting multiple key proteins in the virus life cycle could improve antiviral efficacy. For example, combination therapy using nirmatrelvir and molnupiravir, a ribonucleoside analog, displayed better antiviral efficacy in mice compared with monotherapy with either of these compounds.³⁶ Preclinical studies using combinations of host protease TMPRSS2 inhibitors, including camostat, nafamostat, and avoralstat, with inhibitors of SARS-CoV-2 replication, including molnupiravir, nirmatrelvir, or remdesivir, turned out to be effective (reviewed by Wagoner et al.³⁷). In this study, we designed olgotrelvir and demonstrated its dual mechanism of binding and inhibiting both M^{Pro} and CTSL by co-crystal structures and enzymatic assays, which may present unique advantages in its antiviral activities. Furthermore, olgotrelvir, as a dual inhibitor, may avoid complicated PK, pharmacodynamics, toxicology, and safety properties in clinical applications of combination therapies using two drugs with different mechanisms of action.

A few small molecules have been reported to have dual targets for inhibition of SARS-CoV-2, mostly by inhibiting both M^{Pro} and host CTSL, including MPI8,^{18,38}

GC376, calpain inhibitors II and XII,^{18,39} MG-132,⁴⁰ and SM141.⁴¹ Among them, MPI8 and GC376 are more potent in inhibition of both M^{Pro} and CTSL in *in vitro* assays, with IC₅₀ values for M^{Pro} reported as 105 and 30 nM, respectively,³⁸ and IC₅₀ values for CTSL as 1.2 and 0.23 nM, respectively.¹⁸ Only GC376 was tested *in vivo* for anti-viral activity; however, it showed limited efficacy in mouse viral load reduction^{42,43} due to poor metabolic stability and oral PK profile of the compounds. Olgotrelvir emerged as a highly effective anti-SARS-CoV-2 drug with dual targets. The IC₅₀ for wild-type M^{Pro} is 2.44 nM, and that for Omicron M^{Pro} is 14.27 nM (Figure 2A). For CTSL, the IC₅₀ is 0.06 nM (Figure 2D). Correspondingly, olgotrelvir displayed potent antiviral activities in cell-based assays (Figure 2C; Data S7) and potent activity inhibiting Spike pseudotyped virus entry (Figure 2E). The dual mechanism was also tested in Vero E6 cells and Vero E6 cells overexpressing TMPRSS2 challenged with a WA-1 strain that uses the TMPRSS2 entry pathway and an Omicron BA.5 strain that uses the CTSL entry pathway^{12–14} (Data S8B). Olgotrelvir was more potent in inhibiting Omicron BA.5 than the WA-1 strain in Vero E6 cells, and the potency was decreased in Vero E6 TMPRSS2 cells against BA.5 but not against WA-1 (Data S7B). In mouse models expressing human ACE2 in the lung epithelium, olgotrelvir greatly reduced lung virus titer and pathology and reversed virus infection-associated weight loss (Figure 3).

Accelerated generation of new viral variants is a major concern for patients treated with molnupiravir, a known virus mutagen.⁴⁴ For nirmatrelvir, pre-existing drug resistance has already been found in clinical samples.^{8,45} Especially, a *de novo* E166V/L50V mutation was identified in an immunocompromised patient treated with prolonged nirmatrelvir/RTV monotherapy, leading to clinical and virological treatment failure.⁴⁶ Notably, olgotrelvir and its active form AC1115 were designed to make them versatile to fit in the M^{Pro} catalytic pockets, a target that has proven to be highly conserved across the duration of the ongoing pandemic (Figure 1). Thus, AC1115 displayed inhibition activity against mutants that showed resistance to nirmatrelvir, an M^{Pro} inhibitor and the antiviral component of Paxlovid (Data S9). In addition, the host-encoded olgotrelvir target CTSL is a human protease that will not be affected by virus mutation except for mutations that lead to the abandonment of this entry pathway. The probability of viral mutations altering both M^{Pro} sensitivity to olgotrelvir while keeping the activity and altering the virus entry pathway is very low. Not surprisingly, olgotrelvir and AC1115 displayed broad antiviral activity against all tested SARS-CoV-2 variants in *in vitro* assays (Figure 2; Data S5 and S7). Therefore, olgotrelvir, with the mechanism of dual target inhibition, may not only enhance the antiviral activity but also reduce potential drug resistance originating from virus-encoded mutations.

For the peptidomimetic class of protease inhibitors, the major development risks for oral drug candidates are bioavailability and toxicity.^{47,48} Peptidomimetic compounds are generally metabolically unstable and often result in short serum t_{1/2} and poor oral bioavailability. GC376 and MPI8 are typical cases due to the flexible conformation of the molecules, especially the N-terminal protection group (benzyl). By introducing a bulky group, such as an indole ring, to replace the benzyl group of GC376 and MPI8, the conformation flexibility and peptide character of the molecule were reduced, which led to significant improvement in the metabolic stability and the PK profile of olgotrelvir/AC1115 (Data S24). Nirmatrelvir, the first oral peptidomimetic inhibitor approved for treatment of COVID-19, showed poor bioavailability in humans. The need for RTV to boost nirmatrelvir plasma concentrations creates significant challenges in clinical practice due to DDI risks. Recently, a non-peptidomimetic SARS-CoV-2 M^{Pro} inhibitor, ensitrelvir

(S-217622), was approved in Japan as a standalone treatment of COVID-19.⁴⁹ Although there is no need for RTV to boost ensitrelvir plasma concentration, ensitrelvir itself is a strong CYP 3A4 inhibitor, which could increase the potential for DDIs.⁵⁰

Olgotrelvir exhibited low to moderate bioavailability in rodents and moderate to high bioavailability in non-rodents with an F value of 84% in dogs (Table 2). High plasma exposure of AC1115 in non-rodents and favorable elimination half-lives indicated a PK profile in these models that did not require RTV to achieve durable therapeutic levels of exposure in plasma. In humans, following single oral administration of olgotrelvir at dose levels between 300 mg and 2000 mg (SAD portion of the study), a favorable plasma exposure of AC1115 was observed, with AUC ranging from 14,200 to 94,900 h·ng/mL (Figure 4A, bottom). In the MAD portion of the study, with 7.5 consecutive days of repeated administration of olgotrelvir between 300 mg BID and 800 mg BID, a steady state of plasma concentration of AC1115 was reached, and no accumulation of olgotrelvir was seen (Figure 4B). Moreover, plasma concentrations of AC1115 increased proportionally to increased oral doses in the SAD portion and MAD portion of the study. Notably, the plasma concentration of AC1115 observed in individuals administered a single 600-mg dose of olgotrelvir equaled and exceeded the efficacious concentration of AC1115 measured in the mouse model (Figure 3). These results strongly suggest that olgotrelvir has the potential to be used as a standalone treatment for COVID-19. In addition, our data demonstrated that olgotrelvir is not an inhibitor of CYP3A4 (Data S15 and S16) and therefore carries a reduced risk of DDIs. Olgotrelvir was well tolerated, with no adverse findings in either rats or dogs. The corresponding no observed adverse effect levels (NOAELs) were the highest doses tested (150 mg/kg/day in dogs and 2,000 mg/kg/day in rats).

Although the dual inhibition of both M^{Pro} and CTSL by olgotrelvir is confirmed by co-crystal structures, enzymatic assays, and pseudotyped virus entry studies, in our mouse model, we were not able to determine the relative contributions of CTSL inhibition and M^{Pro} inhibition in the antiviral effect of olgotrelvir. Similarly, the clinical benefit of the dual mechanism of action still needs to be fully validated in patients. In addition, safety concerns from potential off-target effects related to inhibition of host CTSL should also be assessed in humans. The safety, tolerability, PK, and antiviral activity of olgotrelvir as a single agent have been studied in two clinical trials in healthy volunteers and COVID-19 patients. In the study with healthy volunteers (ClinicalTrials.gov: NCT05364840), olgotrelvir is tolerable. No dose limited toxicity was found in human subjects administered a dose up to 2,000 mg (SAD) or 800 mg BID for 7.5 consecutive days (MAD). The ALT/AST elevation observed in two subjects of the 800 mg BID cohort were mild and transient (grade 1 and 2), although special attention should be paid in later phase trials. In the study with COVID-19 patients (ClinicalTrials.gov: NCT05523739), the antiviral activity was also tested. Preliminary results indicate that olgotrelvir can significantly reduce the viral RNA copy numbers even 48 h after administration (day 3), indicating its fast antiviral activity. A phase III trial (ClinicalTrials.gov: NCT05716425) in mild and moderate COVID-19 patients has been conducted to further assess the efficacy and safety of olgotrelvir.

Conclusions

Olgotrelvir, as a next-generation M^{Pro} inhibitor for treatment of COVID-19, has demonstrated a unique complement of properties, including (1) standalone

treatment without an RTV booster, (2) enhanced antiviral activity with dual inhibition of M^{Pro} and CTSL, and (3) potential for overcoming Paxlovid resistance.

Limitations of the study

Although olgotrelvir has demonstrated potent activity against some nirmatrelvir-resistant mutations *in vitro*, whether such activity can be translated to benefits for treatment of COVID-19 patients is still unknown and remains to be further explored. Potent activity on SARS-CoV-1 M^{Pro} was seen for olgotrelvir; however, we did not conduct systematic studies to test antiviral activities across other coronaviruses.

STAR★METHODS

Detailed methods are provided in the online version of this paper and include the following:

- KEY RESOURCES TABLE
- RESOURCE AVAILABILITY
 - Lead contact
 - Materials availability
 - Data and code availability
- EXPERIMENTAL MODEL AND STUDY PARTICIPANT DETAILS
 - Human participants
 - Animal models
 - Cell lines, primary cells and microbe strains
- METHOD DETAILS
 - Synthetic chemistry
 - Structure biology
 - Inhibition of enzyme activities
 - *In vitro* antiviral assays
 - Released virus load in EpiAirway
 - Pseudovirus entry inhibition assay
 - *In vivo* antiviral testing
 - Generation of CTSL KO cell line
 - Cytotoxicity testing
 - Protease panel inhibition testing
 - AC1115 SAFETYscan47 KdMAX Panel Screening
 - Metabolic stability study
 - Cytochrome P450 reaction phenotyping
 - CYP inhibition
 - Transporter (BCRP) inhibition
 - Evaluation of AC1115 as a potential substrate of BCRP and MDR1
 - Pharmacokinetics
 - General toxicity studies
 - Repeat dose toxicity studies with olgotrelvir
 - Safety pharmacology studies with olgotrelvir
 - *In vivo* micronucleus assessment in rats
 - Bacterial reverse mutation assay with olgotrelvir
 - *In vitro* chromosome aberration test of olgotrelvir in Chinese hamster lung cells
 - First-in-human clinical trial
 - Phase I clinical trial in COVID-19 patients
- QUANTIFICATION AND STATISTICAL ANALYSIS

SUPPLEMENTAL INFORMATION

Supplemental information can be found online at <https://doi.org/10.1016/j.medj.2023.12.004>.

ACKNOWLEDGMENTS

The work was funded by Sorrento Therapeutics, Inc. We thank all participants in the NCT05364840 and NCT05364840 clinical trials. All SARS-CoV-2 virus strains used in this study and Vero E6-TMPRSS2-T2A-ACE2 and A549hACE2 cells were obtained through BEI Resources, NIAID, NIH. We thank the Stanford Synchrotron Radiation Lightsource and the Advanced Light Source at Lawrence Berkeley National Laboratory for synchrotron data collection. We thank Hangzhou Allsino Chemicals Co., Ltd. for supply/manufacturing of olgotrelvir API (GMP) to support all clinical studies.

AUTHOR CONTRIBUTIONS

X.X., H.J., L.M., R.A., and H.L. conceived the project. X.X., L.M., W.X., M.B., and M.R. administered the project. L.M., N.S., X.Z., C.J., C.P., W.X., J.L., M.R., C.A., H.L., and X.X. developed the methodology and protocols. N.S., X.Z., C.J., Y.K., C.P., K.S., C.X., Y.B., L.X., Y.Z., H.Y., S.Q., Y.H., J.S., C.Z., T.L., Y. Li, N.L., Z.Z., O.K., Q.H., and X.X. performed experiments and/or data analyses. W.X., C.A., H.L., W.S., C.W., S.W., Z.L., Y. Lin, and D.S. conducted phase I clinical studies. X.Z. oversaw the statistical analyses. L.K. and L.C. produced critical reagents. J.T. provided support for *in vivo* efficacy experiments. L.M., X.Z., C.J., and X.X. wrote the first draft of the manuscript. Y.K., C.P., L.C., M.R., M.B., and R.A. reviewed and edited the manuscript. X.X. and W.X. had unrestricted access to all data. All authors agreed to submit the manuscript, read and approved the final draft, and take full responsibility for its content, including the accuracy of the data and the fidelity of the trial to the registered protocol and its statistical analysis.

DECLARATION OF INTERESTS

L.M., C.J., Y.K., J.L., Z.Z., L.D., and X.X. are shareholders of Sorrento Therapeutics, Inc. and employees of ACEA Therapeutics, Inc., which is a wholly owned subsidiary of Sorrento Therapeutics, Inc. N.S., C.P., K.S., H.X., L.K., M.R., M.B., and H.J. are employees and shareholders of Sorrento Therapeutics, Inc. X.Z., W.X., C.X., Y.B., L.X., Y.Z., H.Y., S.Q., Y.H., J.S., C.Z., T.L., Y. Li, N.L., Z.L., S.W., C.W., and W.S. are employees of ACEA Pharmaceutical Co. Ltd., a wholly owned subsidiary of ACEA Therapeutics, Inc. R.A. was an employee of Sorrento Therapeutics during the study. Sorrento Therapeutics has filed a PCT application (WO 2022/256434 A1) of the compound structures and the synthesis and the pre-clinical properties of olgotrelvir along with its potential treatment of COVID-19 as an antiviral agent.

Received: June 8, 2023

Revised: August 18, 2023

Accepted: December 3, 2023

Published: January 4, 2024; Corrected online: January 17, 2024

REFERENCES

1. Andrews, N., Stowe, J., Kirsebom, F., Toffa, S., Rickeard, T., Gallagher, E., Gower, C., Kall, M., Groves, N., O'Connell, A.M., et al. (2022). Covid-19 Vaccine Effectiveness against the Omicron (B.1.1.529) Variant. *N. Engl. J. Med.* 386, 1532–1546.
2. Huijberts, A.J., de Gier, B., Hoeve, C.E., de Melker, H.E., Hahné, S.J.M., den Hartog, G., Grobbee, D.E., van de Wijgert, J.H.H.M., van den Hof, S., and Knol, M.J. (2023). Vaccine effectiveness of primary and booster COVID-19 vaccinations against SARS-CoV-2 infection in the Netherlands from 12 July 2021 to 6 June 2022: a prospective cohort study. *Int. J. Infect. Dis.* 133, 36–42.
3. Yang, H., and Rao, Z. (2021). Structural biology of SARS-CoV-2 and implications for therapeutic development. *Nat. Rev. Microbiol.* 19, 685–700.
4. Cho, E., Rosa, M., Anjum, R., Mehmood, S., Soban, M., Mujtaba, M., Bux, K., Moin, S.T., Tanweer, M., Dantu, S., et al. (2021). Dynamic Profiling of beta-Coronavirus 3CL M(pro) Protease Ligand-Binding Sites. *J. Chem. Inf. Model.* 61, 3058–3073.
5. Hoffman, R.L., Kania, R.S., Brothers, M.A., Davies, J.F., Ferre, R.A., Gajiwala, K.S., He, M., Hogan, R.J., Kozminski, K., Li, L.Y., et al. (2020). Discovery of Ketone-Based Covalent Inhibitors of Coronavirus 3CL Proteases for the Potential Therapeutic Treatment of COVID-19. *J. Med. Chem.* 63, 12725–12747.
6. Chaparro, J.D., Cheng, T., Tran, U.P., Andrade, R.M., Brenner, S.B.T., Hwang, G., Cohn, S., Hirata, K., McKerrow, J.H., and Reed, S.L. (2018). Two key cathepsins, TgCPB and TgCPL, are targeted by the vinyl sulfone inhibitor

- K11777 in vitro and in vivo models of toxoplasmosis. *PLoS One* 13, e0193982.
7. Sevrioukova, I.F., and Poulos, T.L. (2010). Structure and mechanism of the complex between cytochrome P4503A4 and ritonavir. *Proc. Natl. Acad. Sci. USA* 107, 18422–18427.
 8. Hu, Y., Lewandowski, E.M., Tan, H., Zhang, X., Morgan, R.T., Zhang, X., Jacobs, L.M.C., Butler, S.G., Gongora, M.V., Choy, J., et al. (2023). Naturally Occurring Mutations of SARS-CoV-2 Main Protease Confer Drug Resistance to Nirmatrelvir. *ACS Cent. Sci.* 9, 1658–1669.
 9. Zhou, Y., Gammeltoft, K.A., Ryberg, L.A., Pham, L.V., Tjørnelund, H.D., Binderup, A., Duarte Hernandez, C.R., Fernandez-Antunez, C., Offersgaard, A., Fahnøe, U., et al. (2022). Nirmatrelvir-resistant SARS-CoV-2 variants with high fitness in an infectious cell culture system. *Sci. Adv.* 8, eadd7197.
 10. Jochmans, D., Liu, C., Donckers, K., Stoycheva, A., Boland, S., Stevens, S.K., De Vita, C., Vanmechelen, B., Maes, P., Trüeb, B., et al. (2023). The Substitutions L50F, E166A, and L167F in SARS-CoV-2 3CLpro Are Selected by a Protease Inhibitor In Vitro and Confer Resistance To Nirmatrelvir. *mBio* 14, e0281522.
 11. Liu, T., Luo, S., Libby, P., and Shi, G.P. (2020). Cathepsin L-selective inhibitors: A potentially promising treatment for COVID-19 patients. *Pharmacol. Ther.* 213, 107587.
 12. Peacock, T.P., Brown, J.C., Zhou, J., Thakur, N., Newman, J., Kugathasan, R., Sukhova, K., Kaforou, M., Bailey, D., and W.S., B. (2022). The SARS-CoV-2 variant, Omicron, shows rapid replication in human primary nasal epithelial cultures and efficiently uses the endosomal route of entry. Preprint at bioRxiv.
 13. Willett, B.J., Grove, J., MacLean, O.A., Wilkie, C., De Lorenzo, G., Furnon, W., Cantoni, D., Scott, S., Logan, N., Ashraf, S., et al. (2022). SARS-CoV-2 Omicron is an immune escape variant with an altered cell entry pathway. *Nat. Microbiol.* 7, 1161–1179.
 14. Hoffmann, M., Kleine-Weber, H., Schroeder, S., Krüger, N., Herrler, T., Erichsen, S., Schiergens, T.S., Herrler, G., Wu, N.H., Nitsche, A., et al. (2020). SARS-CoV-2 Cell Entry Depends on ACE2 and TMPRSS2 and Is Blocked by a Clinically Proven Protease Inhibitor. *Cell* 181, 271–280.e8.
 15. Koch, J., Uckele, Z.M., Doldan, P., Stanifer, M., Boulant, S., and Lozach, P.Y. (2021). TMPRSS2 expression dictates the entry route used by SARS-CoV-2 to infect host cells. *EMBO J.* 40, e107821.
 16. Meng, B., Abdullahi, A., Ferreira, I.A.T.M., Goonawardane, N., Saito, A., Kimura, I., Yamasoba, D., Gerber, P.P., Fathi, S., Rathore, S., et al. (2022). Altered TMPRSS2 usage by SARS-CoV-2 Omicron impacts infectivity and fusogenicity. *Nature* 603, 706–714.
 17. Mellott, D.M., Tseng, C.T., Drelich, A., Fajtová, P., Chenna, B.C., Kostomiris, D.H., Hsu, J., Zhu, J., Taylor, Z.W., Kocurek, K.I., et al. (2021). A Clinical-Stage Cysteine Protease Inhibitor blocks SARS-CoV-2 Infection of Human and Monkey Cells. *ACS Chem. Biol.* 16, 642–650.
 18. Ma, X.R., Alugubelli, Y.R., Ma, Y., Vatansever, E.C., Scott, D.A., Qiao, Y., Yu, G., Xu, S., and Liu, W.R. (2022). MPI8 is Potent against SARS-CoV-2 by Inhibiting Dually and Selectively the SARS-CoV-2 Main Protease and the Host Cathepsin L. *ChemMedChem* 17, e202100456.
 19. Sacco, M.D., Ma, C., Lagarias, P., Gao, A., Townsend, J.A., Meng, X., Dube, P., Zhang, X., Hu, Y., Kitamura, N., et al. (2020). Structure and inhibition of the SARS-CoV-2 main protease reveal strategy for developing dual inhibitors against M(pro) and cathepsin L. *Sci. Adv.* 6, eabe0751.
 20. Jin, Z., Du, X., Xu, Y., Deng, Y., Liu, M., Zhao, Y., Zhang, B., Li, X., Zhang, L., Peng, C., et al. (2020). Structure of M(pro) from SARS-CoV-2 and discovery of its inhibitors. *Nature* 582, 289–293.
 21. Zhang, L., Lin, D., Sun, X., Curth, U., Drosten, C., Sauerhering, L., Becker, S., Rox, K., and Hilgenfeld, R. (2020). Crystal structure of SARS-CoV-2 main protease provides a basis for design of improved alpha-ketoamide inhibitors. *Science* 368, 409–412.
 22. Pettersen, E.F., Goddard, T.D., Huang, C.C., Couch, G.S., Greenblatt, D.M., Meng, E.C., and Ferrin, T.E. (2004). UCSF Chimera—a visualization system for exploratory research and analysis. *J. Comput. Chem.* 25, 1605–1612.
 23. Owen, D.R., Allerton, C.M.N., Anderson, A.S., Aschenbrenner, L., Avery, M., Berritt, S., Boras, B., Cardin, R.D., Carlo, A., Coffman, K.J., et al. (2021). An oral SARS-CoV-2 M(pro) inhibitor clinical candidate for the treatment of COVID-19. *Science* 374, 1586–1593.
 24. Ullrich, S., Ekanayake, K.B., Otting, G., and Nitsche, C. (2022). Main protease mutants of SARS-CoV-2 variants remain susceptible to nirmatrelvir. *Bioorg. Med. Chem. Lett.* 62, 128629.
 25. FDA, U.S. (2023). Fact Sheet for Healthcare Providers: Emergency Use Authorization for Paxlovid. <https://www.fda.gov/media/155050/download>.
 26. Iketani, S., Mohri, H., Culbertson, B., Hong, S.J., Duan, Y., Luck, M.I., Annavaiahala, M.K., Guo, Y., Sheng, Z., Uhlemann, A.C., et al. (2023). Multiple pathways for SARS-CoV-2 resistance to nirmatrelvir. *Nature* 613, 558–564.
 27. Clayton, J., de Oliveira, V.M., Ibrahim, M.F., Sun, X., Mahinthichaichan, P., Shen, M., Hilgenfeld, R., and Shen, J. (2023). Integrative Approach to Dissect the Drug Resistance Mechanism of the H172Y Mutation of SARS-CoV-2 Main Protease. *J. Chem. Inf. Model.* 63, 3521–3533.
 28. Heilmann, E., Costacurta, F., Moghadasi, S.A., Ye, C., Pavan, M., Bassani, D., Volland, A., Ascher, C., Weiss, A.K.H., Bante, D., et al. (2023). SARS-CoV-2 3CL(pro) mutations selected in a VSV-based system confer resistance to nirmatrelvir, ensitrelvir, and GC376. *Sci. Transl. Med.* 15, eabq7360.
 29. Lan, S., Neilsen, G., Slack, R.L., Cantara, W.A., Castaner, A.E., Liorson, Z.C., Lulkin, N., Zhang, H., Lee, J., Cilento, M.E., et al. (2023). Nirmatrelvir Resistance in SARS-CoV-2 Omicron_BA.1 and WA1 Replicons and Escape Strategies. Preprint at bioRxiv.
 30. Hammond, J., Leister-Tebbe, H., Gardner, A., Abreu, P., Bao, W., Wisemandle, W., Baniecki, M., Hendrick, V.M., Damle, B., Simón-Campos, A., et al. (2022). Oral Nirmatrelvir for High-Risk, Nonhospitalized Adults with Covid-19. *N. Engl. J. Med.* 386, 1397–1408.
 31. Wang, L., Berger, N.A., Davis, P.B., Kaelber, D.C., Volkow, N.D., and Xu, R. (2022). COVID-19 rebound after Paxlovid and Molnupiravir during January–June 2022. Preprint at medRxiv.
 32. Pandit, J.A., Radin, J.M., Chiang, D.C., Spencer, E.G., Pawelek, J.B., Diwan, M., Roumani, L., and Mina, M.J. (2023). The COVID-19 Rebound Study: A Prospective Cohort Study to Evaluate Viral and Symptom Rebound Differences in Participants Treated with Nirmatrelvir Plus Ritonavir Versus Untreated Controls. *Clin. Infect. Dis.* 77, 25–31.
 33. Boucau, J., Uddin, R., Marino, C., Regan, J., Flynn, J.P., Choudhary, M.C., Chen, G., Stuckwisch, A.M., Mathews, J., Liew, M.Y., et al. (2023). Characterization of Virologic Rebound Following Nirmatrelvir-Ritonavir Treatment for Coronavirus Disease 2019 (COVID-19). *Clin. Infect. Dis.* 76, e526–e529.
 34. Deo, R., Choudhary, M.C., Moser, C., Ritz, J., Daar, E.S., Wohl, D.A., Greninger, A.L., Eron, J.J., Currier, J.S., Hughes, M.D., et al. (2023). Symptom and Viral Rebound in Untreated SARS-CoV-2 Infection. *Ann. Intern. Med.* 176, 348–354.
 35. Pandit, J.A., Radin, J.M., Chiang, D.C., Spencer, E.G., Pawelek, J.B., Diwan, M., Roumani, L., and Mina, M.J. (2023). The Coronavirus Disease 2019 Rebound Study: A Prospective Cohort Study to Evaluate Viral and Symptom Rebound Differences in Participants Treated With Nirmatrelvir Plus Ritonavir Versus Untreated Controls. *Clin. Infect. Dis.* 77, 25–31.
 36. Jeong, J.H., Chokkakula, S., Min, S.C., Kim, B.K., Choi, W.S., Oh, S., Yun, Y.S., Kang, D.H., Lee, O.J., Kim, E.G., et al. (2022). Combination therapy with nirmatrelvir and molnupiravir improves the survival of SARS-CoV-2 infected mice. *Antivir. Res.* 208, 105430.
 37. Wagoner, J., Herring, S., Hsiang, T.Y., Ianevski, A., Biering, S.B., Xu, S., Hoffmann, M., Pöhlmann, S., Gale, M., Jr., Aittokallio, T., et al. (2022). Combinations of Host- and Virus-Targeting Antiviral Drugs Confer Synergistic Suppression of SARS-CoV-2. *Microbiol. Spectr.* 10, e0333122.
 38. Cao, W., Cho, C.C.D., Geng, Z.Z., Shaabani, N., Ma, X.R., Vatansever, E.C., Alugubelli, Y.R., Ma, Y., Chaki, S.P., Ellenburg, W.H., et al. (2022). Evaluation of SARS-CoV-2 Main Protease Inhibitors Using a Novel Cell-Based Assay. *ACS Cent. Sci.* 8, 192–204.
 39. Hu, Y., Ma, C., Szeto, T., Hurst, B., Tarbet, B., and Wang, J. (2021). Boceprevir, Calpain Inhibitors II and XII, and GC-376 Have Broad-Spectrum Antiviral Activity against Coronaviruses. *ACS Infect. Dis.* 7, 586–597.
 40. Costanzi, E., Kuzikov, M., Esposito, F., Albani, S., Demitri, N., Giabbai, B., Camasta, M., Tramontano, E., Rossetti, G., Zaliani, A., and Storici, P. (2021). Structural and Biochemical Analysis of the Dual Inhibition of MG-132 against SARS-CoV-2 Main Protease (Mpro/3CLpro) and Human Cathepsin-L. *Int. J. Mol. Sci.* 22, 11779.

41. Mondal, S., Chen, Y., Lockbaum, G.J., Sen, S., Chaudhuri, S., Reyes, A.C., Lee, J.M., Kaur, A.N., Sultana, N., Cameron, M.D., et al. (2022). Dual Inhibitors of Main Protease (M(Pro)) and Cathepsin L as Potent Antivirals against SARS-CoV2. *J. Am. Chem. Soc.* *144*, 21035–21045.
42. Cáceres, C.J., Cardenas-Garcia, S., Carnaccini, S., Seibert, B., Rajao, D.S., Wang, J., and Perez, D.R. (2021). Efficacy of GC-376 against SARS-CoV-2 virus infection in the K18 hACE2 transgenic mouse model. *Sci. Rep.* *11*, 9609.
43. Dampalla, C.S., Zheng, J., Perera, K.D., Wong, L.Y.R., Meyerholz, D.K., Nguyen, H.N., Kashipathy, M.M., Battaile, K.P., Lovell, S., Kim, Y., et al. (2021). Postinfection treatment with a protease inhibitor increases survival of mice with a fatal SARS-CoV-2 infection. *Proc. Natl. Acad. Sci. USA* *118*, e2101555118.
44. Wahl, A., Gralinski, L.E., Johnson, C.E., Yao, W., Kovarova, M., Dinnon, K.H., 3rd, Liu, H., Madden, V.J., Krzystek, H.M., De, C., et al. (2021). SARS-CoV-2 infection is effectively treated and prevented by EIDD-2801. *Nature* *591*, 451–457.
45. Moghadasi, S.A., Heilmann, E., Khalil, A.M., Nnabuike, C., Kearns, F.L., Ye, C., Moraes, S.N., Costacurta, F., Esler, M.A., Aihara, H., et al. (2023). Transmissible SARS-CoV-2 variants with resistance to clinical protease inhibitors. *Sci. Adv.* *9*, eade8778.
46. Zuckerman, N.S., Bucris, E., Keidar-Friedman, D., Amsalem, M., and Brosh-Nissimov, T. (2023). Nirmatrelvir resistance - de novo E166V/L50V mutations in an immunocompromised patient treated with prolonged nirmatrelvir/ritonavir monotherapy leading to clinical and virological treatment failure - a case report. *Clin. Infect. Dis.* *45*, ciad494.
47. Turk, B. (2006). Targeting proteases: successes, failures and future prospects. *Nat. Rev. Drug Discov.* *5*, 785–799.
48. Drag, M., and Salvesen, G.S. (2010). Emerging principles in protease-based drug discovery. *Nat. Rev. Drug Discov.* *9*, 690–701.
49. Unoh, Y., Uehara, S., Nakahara, K., Nobori, H., Yamatsu, Y., Yamamoto, S., Maruyama, Y., Taoda, Y., Kasamatsu, K., Suto, T., et al. (2022). Discovery of S-217622, a Noncovalent Oral SARS-CoV-2 3CL Protease Inhibitor Clinical Candidate for Treating COVID-19. *J. Med. Chem.* *65*, 6499–6512.
50. Shimizu, R., Sonoyama, T., Fukuhara, T., Kuwata, A., Matsuo, Y., and Kubota, R. (2022). Safety, Tolerability, and Pharmacokinetics of the Novel Antiviral Agent Ensitrelvir Fumaric Acid, a SARS-CoV-2 3CL Protease Inhibitor, in Healthy Adults. *Antimicrob. Agents Chemother.* *66*, e0063222.
51. Battye, T.G.G., Kontogiannis, L., Johnson, O., Powell, H.R., and Leslie, A.G.W. (2011). iMOSFLM: a new graphical interface for diffraction-image processing with MOSFLM. *Acta Crystallogr. D Biol. Crystallogr.* *67*, 271–281.
52. Evans, P.R., and Murshudov, G.N. (2013). How good are my data and what is the resolution? *Acta Crystallogr. D Biol. Crystallogr.* *69*, 1204–1214.
53. McCoy, A.J., Grosse-Kunstleve, R.W., Adams, P.D., Winn, M.D., Storoni, L.C., and Read, R.J. (2007). Phaser crystallographic software. *J. Appl. Crystallogr.* *40*, 658–674.
54. Winn, M.D., Ballard, C.C., Cowtan, K.D., Dodson, E.J., Emsley, P., Evans, P.R., Keegan, R.M., Krissinel, E.B., Leslie, A.G.W., McCoy, A., et al. (2011). Overview of the CCP4 suite and current developments. *Acta Crystallogr. D Biol. Crystallogr.* *67*, 235–242.
55. Adams, P.D., Afonine, P.V., Bunkóczi, G., Chen, V.B., Davis, I.W., Echols, N., Headd, J.J., Hung, L.W., Kapral, G.J., Grosse-Kunstleve, R.W., et al. (2010). PHENIX: a comprehensive Python-based system for macromolecular structure solution. *Acta Crystallogr. D Biol. Crystallogr.* *66*, 213–221.
56. Emsley, P., and Cowtan, K. (2004). Coot: model-building tools for molecular graphics. *Acta Crystallogr. D Biol. Crystallogr.* *60*, 2126–2132.
57. Afonine, P.V., Grosse-Kunstleve, R.W., Echols, N., Headd, J.J., Moriarty, N.W., Mustyakimov, M., Terwilliger, T.C., Urzhumtsev, A., Zwart, P.H., and Adams, P.D. (2012). Towards automated crystallographic structure refinement with phenix.refine. *Acta Crystallogr. D Biol. Crystallogr.* *68*, 352–367.
58. Murshudov, G.N., Skubák, P., Lebedev, A.A., Pannu, N.S., Steiner, R.A., Nicholls, R.A., Winn, M.D., Long, F., and Vagin, A.A. (2011). REFMAC5 for the refinement of macromolecular crystal structures. *Acta Crystallogr. D Biol. Crystallogr.* *67*, 355–367.
59. Duty, J.A., Kraus, T., Zhou, H., Zhang, Y., Shaabani, N., Yildiz, S., Du, N., Singh, A., Miorin, L., Li, D., et al. (2022). Discovery and intranasal administration of a SARS-CoV-2 broadly acting neutralizing antibody with activity against multiple Omicron subvariants. *Méd.* *3*, 705–721.e11.

STAR★METHODS

KEY RESOURCES TABLE

REAGENT or RESOURCE	SOURCE	IDENTIFIER
Antibodies		
Anti SARS-CoV-2 NP	Sorrento Therapeutics	N/A
anti-SARS-CoV-2 Spike	Sorrento Therapeutics	STI-9167
Cathepsin L Monoclonal Antibody (33-2)	ThermoFisher	Cat#BMS1032; RRID:AB_10596643
anti-human b-actin	Sino Biological	Cat#100166-MM10-50; RRID:AB_2860060
Anti-mouse IgG, HRP-linked Antibody	Cell Signaling	Cat#7076; RRID:AB_330924
Alexa Fluor 488 conjugated goat anti-mouse IgG	ThermoFisher	Cat#A-11001; RRID:AB_2534069
anti-VSV-G clone 8G5F11	Millipore	Cat#MABF2337; RRID:AB_2811223
Bacterial and virus strains		
SARS-CoV-2 WA-1	BEI Resources	Cat#NR-52281
SARS-CoV-2 Alpha; lineage B.1.1.7	BEI Resources	Cat#NR-54000
SARS-CoV-2 Beta; lineage B.1.351	BEI Resources	Cat#NR-54009
SARS-CoV-2 Gamma; lineage P.1 (B.1.1.28.1)	BEI Resources	Cat#NR-54982
SARS-CoV-2 Delta; lineage B.1.617.2	BEI Resources	Cat#NR- 55611
SARS-CoV-2 Lambda; lineage C.37	BEI Resources	Cat#NR- 55654
SARS-CoV-2 Omicron BA.1 (B.1.1.529)	BEI Resources	Cat#NR-56461
SARS-CoV-2 Omicron BA.2.12.1	BEI Resources	Cat#NR-56781
SARS-CoV-2 Omicron BA.5	BEI Resources	Cat#NR-56798
<i>E. coli</i> BL21(DE3)	Agilent	Cat#200131
Biological samples		
Human (custom pool of 200 donors, mixed-gender) liver microsomes	XenoTech	Cat#H2610/H0610
Rat (male and female, Sprague Dawley) liver microsomes	XenoTech	Cat#R1000, R1500
Dog (male and female, Beagle) liver microsomes	XenoTech	Cat#D1000, D1500
Mouse (male and female, CD-1) liver microsomes	XenoTech	Cat#M1000, M1500
Monkey (male and female, Cynomolgus) liver microsomes	XenoTech	Cat#P1000, P1500
Human plasma, K ₂ -EDTA	Hangzhou ACEA Pharmaceutical Research Co., Ltd.	N/A
Rat (Sprague Dawley) plasma, K ₂ -EDTA	Hangzhou ACEA Pharmaceutical Research Co., Ltd.	N/A
Dog (Beagle) plasma, K ₂ -EDTA	Medicilon LLC. (Shanghai, China)	N/A
Monkey (Cynomolgus) plasma, K ₂ -EDTA	Medicilon LLC. (Shanghai, China)	N/A
Chemicals, peptides and recombinant proteins		
AC1115	Sorrento Therapeutics	this manuscript
olgotrelvir	Sorrento Therapeutics	
nirmatrelvir	Biochempartner	CAS No: 2628280-40-8, Lot# 20210512, 20211012, 20210725, 20210812
camostat	Fisher Scientific	Cat#50-205-0539
E-64D	BPS	component in cat# 79591
Phenacetin	Aladdin	Cat#P109420
Bupropion	Meilun Bio.	Cat#MB7599
Paclitaxel	Aladdin	Cat#P106869
Diclofenac	Tokyo Chemical Industry (TCI)	Cat#D3748
Mephenytoin	MedChemExpress	Cat#HY-B1184/CS-4793
Dextromethorphan-HBr	National Institutes for Food and Drug	CAS: 6700-34-1
Testosterone	Aladdin	Cat#T102169
NADPH Tetrasodium Salt	Roche Diagnostic	Cat#10621706001
β-NADPH	Sigma-Aldrich	Cat#N7505-100MG
Ketoconazole	J&K Scientific	Cat#973125
Lucifer yellow	Sigma	Cat#L0259

(Continued on next page)

Continued

REAGENT or RESOURCE	SOURCE	IDENTIFIER
N-methylquinidine	Sigma	Cat#SBNMQ
Novobiocin	Sigma	Cat#74675
Cyclosporine A	TCI	Cat#C2408
α -Naphthoflavone	Sigma-Aldrich	Cat#N5757
Thio-TEPA	MedChem Express	Cat#HY-17574
Quercetin	Sigma-Aldrich	Cat#Q4951
Sulfaphenazole	J&K Scientific	Cat#178125
Ticlopidine	Sigma-Aldrich	Cat#T6654
Quinidine	Energy Chemical	CAS: 56-54-2
PEG 400	Sigma-Aldrich	Cat#91893-1L-F
Labrasol ALF	Gattefosse	Lot# 182061
Poloxamer 124	Spectrum Chemical Mfg Corp	Lot# 1H10844
Recombinant human CYP enzymes (1A2, 2B6, 2C8, 2D6, 2C9, 2C19, 3A4)	Cypex	Cat#: CYP/EZ001, CYP/EZ020, CYP/EZ017, CYP/EZ006, CYP/EZ008, CYP/EZ007, CYP/EZ002
Recombinant SARS-CoV-2 M ^{Pro} mutants	BPS Biosciences	this manuscript
Mouse (CD-1), K ₂ -EDTA	Hangzhou ACEA Pharmaceutical Research Co., Ltd.	N/A
5% Glucose injection (D5W)	Chimin Health Management Co., Ltd.	Lot# 210202A02
Critical commercial assays		
3CL Protease, untagged (SARS-CoV-2) assay kit	BPS Biosciences	Cat#78042-2
3CL Protease (Omicron, SARS-CoV-2) assay kit	BPS Biosciences	Cat#78350-2
Cathepsin L Inhibitor Screening Assay Kit	BPS Biosciences	Cat#79591
Cathepsin B Inhibitor Screening Assay Kit	BPS Biosciences	Cat#79590
Cathepsin S Inhibitor Screening Assay Kit	BPS Biosciences	Cat#79588
Cathepsin V Inhibitor Screening Assay Kit	BPS Biosciences	Cat#79589
Cathepsin F Inhibitor Screening Assay Kit	BPS Biosciences	Cat#79971
Cathepsin K Inhibitor Screening Assay Kit	BioVision	Cat#K150-100
Vesicular Transporter Assay Reagent Kit	GenoMembrane (Japan)	Cat#GM3010
Cell Line Nucleofector Kit L	Lonza	Cat#VCA-1005
Bio-Plex Pro Mouse Cytokine 23-plex Assay	Biorad	Cat#171000201
CellTiter-Glo®	Promega	Cat#G7572
ONE-Glo E6120	Promega	Cat#498848
Cell Line Nucleofector Kit L	Lonza	Cat#VCA-1005
Vesicular Transporter Assay Reagent Kit	GenoMembrane (Japan)	Cat#GM3010
Deposited data		
Raw and analyzed data	This paper	N/A
Experimental models: Cell lines		
Vero E6	ATCC	Cat#CRL-1586
Vero E6 -TMPRSS2-T2A-ACE2	BEI	Cat#NR-54970
A549hACE2	BEI	Cat#NR-53821
HEK Blue-hACE2	Invivogen	Cat#hkb-hace2
HEK Blue-hACE2-TMPRSS2	Invivogen	Cat#hkb-hace2tpsa
A549	ATCC	Cat#CCL-185
ARPE19	ATCC	Cat#CRL-2302
ACHN	ATCC	Cat#CRL-1611
Beas-2B	ATCC	Cat#CRL-9609
HepG2	ATCC	Cat#HB-8065
H4	ATCC	Cat#HTB-148
Caco-2	ATCC	Cat#HTB-37
BHK21	ATCC	Cat#CCL-10
EpiAirway	Mattek	Cat#Air-100
Experimental models: Organisms/strains		
K18-hACE2 transgenic mice (female)	Jackson laboratory	Strain #:034860
Balb/c mouse (male and female)	Vital River (Zhejiang, China)	N/A
SD rat (male and female)	Vital River (Zhejiang, China)	N/A
Beagle dog (male and female)	Shen Yang Kang Ping Institute of Laboratory Animals (China)	N/A

(Continued on next page)

Continued

REAGENT or RESOURCE	SOURCE	IDENTIFIER
Recombinant DNA		
G-Pseudotyped ΔG-luciferase (G*ΔG-luciferase) rVSV	Kerafast	Cat#EH1025-PM
SARS-CoV-2 Wuhan Spike with D614G	Sino Biological	Cat#VG40589-UT
plasmid pcDNA3.1	ThermoFisher	Cat#V79020
pGEX-6P1	Genscript	N/A
Software and algorithms		
GraphPad	Prism	N/A
Phoenix WinNonlin 8.3	Certara	N/A
Other		
Human MDR1 vesicles	GenoMembrane (Japan)	Cat#GM0015
Human BCRP vesicles	GenoMembrane (Japan)	Cat#GM0008
Rapid Equilibrium Dialysis (RED™) device, couple with 8k molecular weight cutoff membranes	Thermo Scientific	Cat#90006

RESOURCE AVAILABILITY

Lead contact

Further information and requests for resources and reagents should be directed to the lead contact: Xiao Xu (xxu@aceatherapeutics.com)

Materials availability

Request for olgotrelvir shall be directed to: xxu@aceatherapeutics.com, and MTA will need to be signed before the distribution of olgotrelvir.

Data and code availability

- (1) All data reported in this paper may be shared by the lead contact upon request.
- (2) No original code is reported in this paper.
- (3) Any additional information required to reanalyze the data reported in this paper is available from the lead contact upon request.

EXPERIMENTAL MODEL AND STUDY PARTICIPANT DETAILS

Human participants

The Phase I clinical trial in healthy human volunteers protocol (NCT05364840) was approved by Bellberry human research ethics committee of Australia (Application No: 2022-04-380-A-3). The Phase I clinical trial in healthy human volunteers and COVID-19 patients protocol (NCT05523739) was approved by China National Medical Product Administration (NMPA) (Application No: CXHL2200534). These studies were conducted in compliance with the clinical study protocol (and amendments), International Council for Harmonisation of Technical Requirements for Pharmaceuticals for Human Use, Good Clinical Practice, and applicable regulatory requirements.

For the healthy volunteers, participants were required to be healthy adults aged 18–45 years, with a body mass index of 18–30 kg/m² and a body weight between 45 and 100 kg. Exclusion criteria included history of clinically significant hematologic, renal, endocrine, pulmonary, gastrointestinal, cardiovascular, hepatic, psychiatric, neurologic, or allergic disease and conditions affecting drug absorption. A total of 58 participants were randomized in this study (34 subjects in Part 1 SAD and 24 subjects in Part 2 MAD).

For COVID-19 patients, participants were required to be 18–65 years old, gender is not limited, BMI between 18 and 30 kg/m², and weight between 45 and 100 kg. Patients diagnosed as SARS-CoV-2-positive asymptomatic or mild according to the Novel Coronavirus Pneumonia Treatment Protocol (Trial Version 9). Positive SARS-CoV-2 was first

detected in specimens such as nasal or oropharyngeal swabs within 5 days prior to D1 (≤ 5 days from D1) using a nucleic acid amplification assay. Exclusion criteria included history of clinically significant hematologic, renal, endocrine, pulmonary, gastrointestinal, cardiovascular, hepatic, psychiatric, neurologic, or allergic disease and conditions affecting drug absorption, and treatment with anti-COVID-19 drugs.

Participants information on sex, age, and race was self-reported. Information on gender and socioeconomic status was not collected.

Animal models

Mice for in vivo antiviral studies. Female K18-hACE2 transgenic mice were purchased from Jackson laboratory and maintained in pathogen-free conditions and handling conforms to the requirements of the National Institutes of Health and the Scripps Research Institute Animal Research Committee. Eight to twelve-week old mice (weight range of 16.2–29.1 g) were used. Animal experiments were approved by Sorrento Therapeutics, Inc. Protocol approval committee.

Animals for PK and toxicological studies. *In vivo* PK and toxicology studies were conducted in compliance with the Guide for the Care and Use of Laboratory Animals (2011) issued by the National Research Council, USA, the Laboratory Animal Administration (revised in 2017) issued by the State Science and Technology Committee, People's Republic of China, and the Laboratory Animal Administration Regulations (revised in 1997) issued by the Jiangsu Laboratory Animal Administration Office, P. R. China. The care and use of animals in these studies were reviewed and approved by the Institutional Animal Care and Use Committee (IACUC) of the testing facility.

Cell lines, primary cells and microbe strains

Cell lines for in vitro antiviral activity and pseudovirus entry assessment. HEK-Blue hACE2-TMPRSS2 (InvivoGen #hkb-hace2tpsa) and HEK-Blue hACE2 (InvivoGen #hkb-hace2tpsa) were initiated and cultured according to the manufacturer's protocol. Cells were maintained in DMEM medium (Cytiva # SH30243.01) supplemented with 10% heat-inactivated FBS (Thermo Fisher #10438-026) and selection antibiotics: 0.5 $\mu\text{g}/\text{mL}$ puromycin (InvivoGen #ant-pr-1) and 100 $\mu\text{g}/\text{mL}$ zeocin (InvivoGen #ant-zn-1). HEK-Blue hACE2-TMPRSS2 cell media also contained 200 $\mu\text{g}/\text{mL}$ hygromycin b (InvivoGen #ant-hg-1 or Thermo Fisher #10687010). Cathepsin L KO HEK-Blue hACE2-TMPRSS2 were cultured under the same conditions as parental HEK-Blue hACE2-TMPRSS2 cells. A549 hACE2 cells were obtained from BEI resources repository (#NR-53821) and cultured in DMEM media supplemented with 10% FBS (Cytiva # SH30071.03), 1% penicillin and streptomycin (Sigma Aldrich #p4333), and 100 $\mu\text{g}/\text{mL}$ blasticidin (InvivoGen #ant-bl-1). Vero E6 (ATCC #CRL1586) were maintained in DMEM supplemented with 10% FBS. Vero E6-TMPRSS2 (XenoTech #JCRB1819) were maintained in DMEM with 10% FBS, 1% penicillin and streptomycin, and 1 mg/mL Geneticin (G418, Thermo Fisher #10131035). Baby hamster kidney 21 (BHK21) cells (ATCC #CCL-10) were cultured in DMEM/F12 media (Thermo Fisher #21041025) supplemented with 10% FBS (Omega #FB-02) and 5% tryptose phosphate broth (Thermos Fisher #18050039).

Cell lines for cytotoxicity and pre-clinical DMPK study. A549, ARPE19, ACHN, Beas-2B, H4, and HepG2 cell lines were obtained from ATCC and maintained in the basal medium supplemented with 10% fetal bovine serum (FBS; Cytiva # SH30071.03) and 1% penicillin and streptomycin (Sigma Aldrich #p4333). The basal media were: A549 (#CCI-185) - F-12K media (Corning #10-025-CV); H4 - Dulbecco's modified Eagle's minimum essential medium (DMEM, Cytiva # SH30243.01); ARPE-19 (#CRL-2302)

2,5-Dioxopyrrolidin-1-yl 1H-indole-2-carboxylate (2). To a cooled to 0°C solution of 1H-indole-2-carboxylic acid **1** (200 g, 1.24 mol) and N-hydroxy succinimide (157.1 g, 1.37 mol) in DCM (2.5 L) was added EDCI (286 g, 1.49 mmol). After stirring at room temperature (rt) overnight, the solvent was removed under reduced pressure. The resulting solid was triturated with deionized water, and the solid was collected and dried under reduced pressure to give the title compound (**2**) as a light-brown powder (310 g, 96%).

¹H NMR (400 MHz, CDCl₃) δ 9.01 (s, 1H), 7.70 (d, *J* = 8.2 Hz, 1H), 7.49–7.35 (m, 3H), 7.19 (t, *J* = 7.4 Hz, 1H), 2.92 (s, 4H).

Methyl (2S)-2-amino-3-[(3S)-2-oxopyrrolidin-3-yl]propanoate hydrochloride (4). To a stirred at room temperature (rt) mixture of methyl (2S)-2-[[tert-butoxy]carbonyl]amino-3-[(3S)-2-oxopyrrolidin-3-yl]propanoate (**3**) (500 g, 1.75 mol) in MeOH (200 mL) was added 4M HCl in 1,4-dioxane (2 L). The mixture was stirred at rt for 2 h, then the reaction mixture was concentrated under reduced pressure to afford methyl (2S)-2-amino-3-[(3S)-2-oxopyrrolidin-3-yl]propanoate hydrochloride salt (**4**) (389 g, 1.72 mol, 98%) as a light-yellow solid, which was used for next step without further purification. [M + H]⁺: 187.1.

Methyl (S)-2-[(S)-2-[(tert-butoxycarbonyl)amino]-4-methylpentanamido]-3-[(S)-2-oxopyrrolidin-3-yl]propanoate (6). To a stirred at rt mixture of methyl (2S)-2-amino-3-[(3S)-2-oxopyrrolidin-3-yl]propanoate hydrochloride (389 g, 1.72 mol) (**4**) and DIEA (866 mL, 5.24 mol) in DCM (1.8 L) and EtOH (0.5 L) was added 2,5-dioxopyrrolidin-1-yl (2R)-2-[[tert-butoxy]carbonyl]amino-4-methyl-pentanoate (**5**) (573 g, 1.74 mol). The reaction mixture was stirred at rt for 2 h, then washed with water (2 x 1 L), followed by 0.5 M HCl (1.1 L), sat. NaHCO₃ (1 L) and water (1 L). The organic layer was separated, dried with anhydrous Na₂SO₄, filtered and concentrated under reduced pressure to afford the title product (**6**) (700 g, 1.75 mol, >99%) as a light-yellow solid, which was used for the next step without further purification. [M + H]⁺: 400.3.

¹H NMR (400 MHz, DMSO-*d*₆) δ 8.32 (d, *J* = 8.0 Hz, 1H), 7.62 (s, 1H), 6.88 (d, *J* = 8.0 Hz, 1H), 4.40–4.28 (m, 1H), 3.94 (dd, *J* = 15.1, 8.1 Hz, 1H), 3.74–3.52 (m, 3H), 3.15 (t, *J* = 8.8 Hz, 1H), 3.06 (dd, *J* = 16.4, 9.2 Hz, 1H), 2.33 (t, *J* = 9.2 Hz, 1H), 2.14–2.00 (m, 2H), 1.68–1.51 (m, 3H), 1.42–1.34 (m, 11H), 0.87 (dd, *J* = 11.4, 6.6 Hz, 6H).

Methyl (S)-2-[(S)-2-amino-4-methylpentanamido]-3-[(S)-2-oxopyrrolidin-3-yl]propanoate hydrochloride (7). A mixture of methyl (2S)-2-[(2S)-2-[[tert-butoxy]carbonyl]amino]-4-methylpentan-amido-3-[(3S)-2-oxopyrrolidin-3-yl]propanoate (**6**) (590 g, 1.47 mol) in 4N HCl in 1,4-dioxane (3 L) was stirred at rt for 2 h. After completion of the reaction the reaction mixture was concentrated down under reduced pressure to give the title product (**7**) as a yellow solid (490 g, 99%), which was used for the next step without further purification. [M + H]⁺: 300.2.

Methyl (S)-2-[(S)-2-(1H-indole-2-carboxamido)-4-methylpentanamido]-3-[(S)-2-oxopyrrolidin-3-yl]propanoate (8). To a stirred mixture of methyl (S)-2-[(S)-2-amino-4-methylpentanamido]-3-[(S)-2-oxopyrrolidin-3-yl]propanoate hydrochloride (**7**) (418 g, 1235 mmol) and TEA (519 mL, 3.73 mol) in DMF (2.5 L) at rt was added 2,5-dioxopyrrolidin-1-yl 1H-indole-2-carboxylate (**2**) (353 g, 1.37 mol). The reaction mixture was stirred at rt for 1.5 h. Ethyl acetate (EtOAc) (6 L) was added into the reaction mixture, which was then washed with brine (6 x 6 L). The organic layers were combined, dried over anhydrous sodium sulfate, and concentrated down under reduced pressure. The title product

(8) was obtained as an off-white solid (414 g, Y: 76%), which was used for the next step without further purification. $[M + H]^+$: 443.3.

^1H NMR (400 MHz, $\text{DMSO}-d_6$) δ 11.55 (s, 1H), 8.54 (t, $J = 12.2$ Hz, 1H), 8.40 (d, $J = 8.1$ Hz, 1H), 7.62 (d, $J = 8.1$ Hz, 2H), 7.43 (d, $J = 8.2$ Hz, 1H), 7.24 (t, $J = 10.3$ Hz, 1H), 7.18 (t, $J = 7.5$ Hz, 1H), 7.04 (t, $J = 7.5$ Hz, 1H), 4.65–4.50 (m, 1H), 4.44–4.28 (m, 1H), 3.72–3.55 (s, 3H), 3.19–3.06 (m, 2H), 2.36 (ddd, $J = 13.8, 10.3, 4.0$ Hz, 1H), 2.16–2.03 (m, 2H), 1.79–1.49 (m, 5H), 0.92 (dt, $J = 14.4, 7.2$ Hz, 6H).

N-((*S*)-1-(((*S*)-1-hydroxy-3-((*S*)-2-oxopyrrolidin-3-yl)propan-2-yl)amino)-4-methyl-1-oxopentan-2-yl)-1H-indole-2-carboxamide (9). To a cooled to 0°C under inert atmosphere stirred solution of methyl (S)-2-((S)-2-(1H-indole-2-carboxamido)-4-methylpentanamido)-3-((S)-2-oxopyrrolidin-3-yl)propanoate (8) (500 g, 1.13 mol) in THF (20 L) was portion-wise added LiBH_4 (74 g, 3.39 mol). The reaction mixture was stirred at 0°C for 4 h. After completion of the reaction (monitored by LCMS), the reaction mixture was quenched with sat. aqueous NH_4Cl until no more gas formed. The organic layer was separated, washed with brine (4 x 5 L), dried over anhydrous sodium sulfate, filtered and concentrated down under reduced pressure. The resulting residue was purified by silica gel column chromatography (DCM: MeOH = 15 : 1) to give the desired product (9) (310 g, 66%) as a white solid. $[M + H]^+$: 415.2.

^1H NMR (400 MHz, $\text{DMSO}-d_6$) δ 11.57 (s, 1H), 8.39 (d, $J = 8.2$ Hz, 1H), 7.79 (d, $J = 9.0$ Hz, 1H), 7.61 (d, $J = 7.9$ Hz, 1H), 7.52 (s, 1H), 7.42 (d, $J = 8.3$ Hz, 1H), 7.26 (d, $J = 1.4$ Hz, 1H), 7.17 (t, $J = 7.6$ Hz, 1H), 7.03 (t, $J = 7.5$ Hz, 1H), 4.67 (t, $J = 5.6$ Hz, 1H), 4.50 (td, $J = 9.7, 5.0$ Hz, 1H), 3.80 (s, 1H), 3.40–3.28 (m, 1H), 3.28–3.20 (m, 1H), 3.15–2.99 (m, 2H), 2.33–2.20 (m, 1H), 2.12 (dt, $J = 17.8, 9.4$ Hz, 1H), 1.86–1.75 (m, 1H), 1.75–1.64 (m, 2H), 1.56 (ddd, $J = 19.3, 9.6, 6.9$ Hz, 2H), 1.45–1.35 (m, 1H), 0.91 (dd, $J = 15.6, 6.3$ Hz, 6H).

N-((*S*)-4-methyl-1-oxo-1-(((*S*)-1-oxo-3-((*S*)-2-oxopyrrolidin-3-yl)propan-2-yl)amino)pentan-2-yl)-1H-indole-2-carboxamide (10, AC1115). To a stirred at rt solution of *N*-((*S*)-1-(((*S*)-1-hydroxy-3-((*S*)-2-oxopyrrolidin-3-yl)propan-2-yl)amino)-4-methyl-1-oxopentan-2-yl)-1H-indole-2-carboxamide (9) (8.3 g, 20 mmol) in DMSO (60 mL) was added IBX (11.2 g, 40 mmol). The reaction mixture was stirred at 30°C for 18 h then diluted with EtOAc (300 mL) and filtered. The filtrate was washed with mixture of brine and sat. NaHCO_3 (1:1 to 5:1, 5 x 200 mL). The organic layer was separated, dried over anhydrous sodium sulfate, filtered and concentrated down at rt to afford crude product, which was treated with THF (40 mL) overnight at rt. The obtained solid was collected and dried under vacuum to yield the desired product *N*-((*S*)-4-methyl-1-oxo-1-(((*S*)-1-oxo-3-((*S*)-2-oxopyrrolidin-3-yl)propan-2-yl)amino)pentan-2-yl)-1H-indole-2-carboxamide (10, AC1115) as a white solid (2.5 g, 31%). $[M + H]^+$: 413.2.

^1H NMR (400 MHz, CDCl_3) δ 9.75 (s, 1H), 9.49 (s, 1H), 8.64 (s, 1H), 7.62 (d, $J = 8.0$ Hz, 1H), 7.40 (d, $J = 8.4$ Hz, 1H), 7.27 (d, $J = 8.4$ Hz, 1H), 7.14–7.05 (m, 2H), 7.01 (s, 1H), 6.34 (s, 1H), 4.90 (s, 1H), 4.34 (s, 1H), 3.27–3.22 (m, 2H), 2.43 (s, 1H), 2.30 (s, 1H), 2.01–1.96 (m, 1H), 1.94–1.91 (m, 1H), 1.88–1.65 (m, 4H), 1.00–0.98 (m, 6H).

Sodium (2*S*)-2-((*S*)-2-(1H-indole-2-carboxamido)-4-methylpentanamido)-1-hydroxy-3-((*S*)-2-oxopyrrolidin-3-yl)propane-1-sulfonate (11, sodium olgotrelvir). To a stirred solution of *N*-((*S*)-4-methyl-1-oxo-1-(((*S*)-1-oxo-3-((*S*)-2-oxopyrrolidin-3-yl)propan-2-yl)amino)pentan-2-yl)-1H-indole-2-carboxamide (10) (31 g, 75.15 mmol) in EtOAc (300 mL) at room temperature was added a solution of NaHSO_3 (7.56 g,

72.73 mmol) in water (100 mL). The reaction mixture was heated at 50°C for 3 h. After completion of the reaction (monitored by LCMS), the organic layer was separated and removed. The aqueous layer was washed with EtOAc (5 x 100 mL), concentrated down to remove remaining EtOAc, and then lyophilized to provide the desired product sodium (2S)-2-((S)-2-(1H-indole-2-carboxamido)-4-methylpentanamido)-1-hydroxy-3-((S)-2-oxopyrrolidin-3-yl)propane-1-sulfonate (**11**, sodium olgotrelvir) as off-white solid (32 g, 85%). $[M-Na+2H]^+$: 495.2.

1H NMR (400 MHz, DMSO- d_6) δ 11.57 (s, 1H), 8.45 (dd, $J = 20.7, 8.2$ Hz, 1H), 7.72 (dd, $J = 48.9, 9.2$ Hz, 1H), 7.62 (d, $J = 8.1$ Hz, 1H), 7.50–7.38 (m, 2H), 7.25 (dd, $J = 5.1, 1.4$ Hz, 1H), 7.18 (t, $J = 7.6$ Hz, 1H), 7.04 (t, $J = 7.5$ Hz, 1H), 5.43 (dd, $J = 50.7, 5.9$ Hz, 1H), 4.57–4.41 (m, 1H), 4.33–4.03 (m, 1H), 4.01–3.82 (m, 1H), 3.19–2.92 (m, 2H), 2.29–2.08 (m, 2H), 2.06–1.90 (m, 1H), 1.83–1.51 (m, 5H), 1.00–0.83 (m, 6H).

Structure biology

Expression and purification of M^{Pro} for crystallization study. The synthetic cDNA coding for the M^{Pro} enzyme from the SARS-CoV-2 virus (Wuhan-Hu-1 isolate; accession number MN908947), optimized for *Escherichia coli* (*E. Coli*) expression, was cloned into the pGEX-6P1 vector (Genscript). Its C-terminal contains hexahistidine affinity tag, SGVTFQ↓GPHHHHHH, which is a modified PreScission cleavage site. Purified expression vector was transformed into BL21(DE3) *E. coli* strain (Agilent, Santa Clara, CA) by heat-shock transformation. Inoculum culture was grown in a shake flask containing 50 mL of LB medium plus ampicillin at 37°C overnight, and further amplified in 1.5 L shake flasks to an optical density of 0.5 at 600 nm at 37°C. The expression was induced by addition of 0.5 mM isopropyl β -D-thiogalactopyranoside (IPTG) for 16 h at 16°C, after which the culture was spun down and resultant pellets were stored at –80°C. For purification of authentic M^{Pro}, frozen pellets were resuspended in Buffer A (20 mM Tris-HCl, 150 mM NaCl, 10% glycerol, 5 mM beta-mercaptoethanol, pH 7.8) and lysed via sonication and clarified by centrifugation at 12,000 g for 30 min at 4°C. Clarified lysate was supplemented with Buffer B (20 mM Tris, 150 mM NaCl, 500 mM imidazole, 10% glycerol, pH 7.8, 5mM beta-mercaptoethanol) to 40 mM imidazole then loaded at 2 mL/min⁻¹ onto a 5mL Ni-Trap (GE) column equilibrated in Buffer A with 10% Buffer B. The column was washed with 10% Buffer B, followed by elution of M^{Pro} with 80% Buffer B. PreScission protease (1:20) was added to the eluate, then dialyzed against Buffer C (20 mM Tris, 150 mM NaCl, 1 mM EDTA, 1 mM DTT, pH 7.8) at 4°C overnight. PreScission protease and undigested protein were removed from the sample by passage through GST-gravity and Ni-gravity columns. The authentic, mature M^{Pro} enzyme was concentrated and loaded onto a Superdex S-200 column (GE) equilibrated in Buffer C using an Akta purifier (GE). Eluted protein was concentrated via Amicon concentrator to 7.2 mg/mL, frozen in liquid nitrogen and stored at –80°C.

Co-crystallization, data collection and structure solution of M^{Pro} with AC1115. SARS-CoV-2 M^{Pro} protein (7.20 mg/mL) was crystallized by vapor diffusion. Well solution (0.1 M imidazole pH 8, 0.1 M LiSO₄, 1 mM DTT, 12–16% PEG3000) mixed in a 1:1 (v/v) ratio with protein was set up with hanging drop plates. Small crystalline plates were generated after 1–3 days. Drops containing crystals were crushed and diluted in well solution to prepare seed stocks. Fresh hanging drops were prepared and mixed with seed dilutions (1:1:0.5 protein:well solution:seed dilution (v/v:v)). Large plate crystals grew overnight. Crystals were transferred into 1 mM compound soaking solution (Buffer C mixed 1:1 with well solution, supplemented with 40 mM compound in DMSO). After 8 to 24 h, soaked crystals were washed in well solution

with 20% glycerol as a cryoprotectant, then frozen in liquid nitrogen and stored for data collection. X-ray diffraction datasets were collected on Beamline 5.0.2 of the Advanced Light Source (ALS) at Lawrence Berkeley National Laboratory using a Pilatus3 6M 25 Hz detector and processed using DIALS in the xia2 module of the CCP4 Suite.⁵¹ Data was merged and scaled with Aimless.⁵² Structure solution was carried out by molecular replacement via Phaser using apo SARS-CoV-2 M^{Pro} (PDB: 7bro) as a search model.⁵³ The compound was built in JLigand and fit into the Fo-Fc electron density map.⁵⁴ Iterative rounds of model building in Coot⁵⁵ and refinement in Refmac⁵⁶ and Phenix⁵⁷ generated the final model analyzed by Molprobit⁵⁸ to generate the final statistics table.

Diffraction Data and Refinement Statistics.

Compound	AC1115
Protein	SARS-CoV-2 M ^{Pro}
PDB entry ID	8UAB
Wavelength (Å)	1.0
Resolution	48.2–1.78
Space group	I ₁ 2 ₁
Unit cell dimensions [Å]	a = 45.9, b = 53.4, c = 113.4
Unit cell dimensions [°]	α = 90.0, β = 101.1, γ = 90.0
Total number of reflections ^a	172244 (9893)
Unique reflections ^a	25214 (1428)
Multiplicity ^a	6.8 (6.9)
Completeness (%) ^a	97.6 (97.2)
Mean I/σ(I) ^a	10.9 (0.8)
R _{merge} ^b	0.088 (2.259)
R _{pim} ^c	0.036 (0.912)
CC _{1/2} ^d	0.999 (0.429)
Refinement Statistics	
Reflections used	23182
Reflections used for R _{free}	1996
R _{cryst} ^e	0.1916
R _{free}	0.2286
Ramachandran Plot	
Favored regions (%)	98.68
Allowed Regions (%)	0.99
Outlier regions (%)	0.33

a Numbers in parentheses refer to the highest resolution shell.

b $R_{\text{merge}} = \frac{\sum \sum |I_i - \langle I \rangle|}{\sum \sum I_i}$

c $R_{\text{pim}} = \frac{\sum \sqrt{1 - I_i} \sum |I_i - \langle I \rangle|}{\sum \sum I_i}$

d CC_{1/2} = as defined by Karplus and Diederichs

e $R_{\text{cryst}} = \frac{\sum |F_o - F_c|}{\sum F_o}$, where F_o and F_c are the observed and calculated structure factors, respectively.

R_{free} is the same as R_{cryst}, but for 7.9% of the data randomly omitted from refinement.

Expression, refolding and purification of CTSL for crystallization study. The gene coding for hCTSL was subcloned from the pDONR201-hCTSL vector (DNASU plasmid repository) into the pET28a vector (EMD Millipore). Upon sequence verification, the pET28a vector encoding CTSL was transformed into BL21(DE3) *E. coli* strain (Agilent) and the transformed culture was incubated at 37°C with shaking until reaching an OD₆₀₀ of 0.6, at which time protein expression was induced through the addition of IPTG and continued incubation at 33°C overnight. Harvested bacterial pellets were lysed via sonication in lysis buffer (50 mM Tris-Cl pH 8.0, 2 mM EDTA, 5% sucrose) and the resultant lysate was spun down at 17000 g for 30 min at 4°C. The inclusion body pellet containing CTSL was washed via sonication in 50 mM Tris-Cl pH 8.0, 2 mM EDTA, 0.1% Triton X-100 followed by centrifugation. The inclusion body wash was repeated with 50 mM Tris-Cl pH 8.0, 1 M urea before the inclusion body was solubilized in 50 mM Tris-Cl pH 8.0, 5 mM EDTA, 6 M GuHCl, 0.15 M NaCl, 10 mM DTT. Refolding buffer (50 mM Tris-Cl pH 8.5, 0.5 M arginine, 0.01% Brij35, 0.01 M NaCl, 10 mM GSH, and 1 mM GSSG) was gradually added (0.5 mL/min) to the sample at 4°C and the mixture was stirred for at least 48 h before dialysis against 25 mM Na₃PO₄ pH 7.0, 500 mM NaCl. After diluting and supplementing the sample with glycerol to a final composition of 25 mM Na₃PO₄ pH 7.0, 250 mM NaCl, 5% glycerol, the sample was incubated with Ni²⁺-agarose beads (Marvelgent Biosciences) overnight at 4°C. The beads were washed with buffer (25 mM Na₃PO₄ pH 7.0, 250 mM NaCl, 5% glycerol) before elution with the same buffer supplemented with 500 mM imidazole. Fractions containing CTSL were combined and dialyzed into 20 mM NaAc pH 4.0, 0.3 M NaCl, 5 mM DTT, 2.5 mM EDTA, 0.01% NaN₃. To initiate autocleavage, 20 mM cysteine was added to CTSL and the sample was incubated at 45°C for 30 min. Cleaved protein was concentrated to 2 mg/mL for further use in crystallization trials.

Co-crystallization, data collection and structure solution of CTSL with AC1115. CTSL (2 mg/mL) was incubated overnight with AC1115 (1 mM) and the following day the resultant complex was exchanged into 20 mM Bis-tris pH 7.0, 100 mM NaCl, 5% glycerol, 5 mM DTT, 0.01% NaN₃ through several cycles of concentration and re-suspension in a centrifugal filter (Amicon). Concentrated CTSL-AC1115 complex (23.3 mg/mL) crystallized in a hanging drop plate with 0.1 M NaOAc, pH 5.5, 25% PEG 3350 (0.5 μL protein:0.5 μL well drop ratio). The crystals were cryoprotected in well solution supplemented with 20% glycerol prior to flash freezing and storage in liquid nitrogen.

X-ray diffraction datasets were collected on Beamline 12-1 at the Stanford Synchrotron Radiation Light source using an Eiger 16M detector, indexed, integrated, and reduced with iMOSFLM,⁵¹ and scaled with Aimless.⁵² Phaser TNCS⁵³ from the CCP4 suite⁵⁴ was used to account for translational noncrystallographic symmetry. Molecular replacement was done with Phaser from the Phenix suite⁵⁵ for initial phase determination using CTSL (PDB: 6ezp) as a search model. The protein structure was modeled against the data via iterative rounds of manual fitting in Coot.⁵⁶ with subsequent refinement in Phenix.refine⁵⁷ and refmac5.⁵⁸

Diffraction Data and Refinement Statistics.

Compound	AC1115
Protein	Human CTSL
PDB entry ID	8UAC

(Continued on next page)

Continued	
Compound	AC1115
Wavelength (Å)	1.0
Resolution	61.32–1.40
Space group	P2 ₁ 2 ₁ 2 ₁
Unit cell dimensions [Å]	a = 45.9, b = 76.4, c = 102.7
Unit cell dimensions [°]	α = 90.0, β = 90.0, γ = 90.0
Total number of reflections ^a	841428 (42270)
Unique reflections ^a	71556 (3493)
Multiplicity ^a	11.8 (12.1)
Completeness (%) ^a	99.6 (99.7)
Mean I/σ(I) ^a	6.6 (0.6)
R _{merge} ^b	0.169 (4.146)
R _{pim} ^c	0.074 (1.803)
CC _{1/2} ^d	0.997 (0.614)
Refinement Statistics	
Reflections used	59071
Reflections used for R _{free}	3101
R _{cryst} ^e	0.2093
R _{free}	0.2440
Ramachandran Plot	
Favored regions (%)	96.67
Allowed Regions (%)	3.33
Outlier regions (%)	0.00

^aNumbers in parentheses refer to the highest resolution shell.

^b $R_{\text{merge}} = \frac{\sum \sum |I_i - \langle I \rangle|}{\sum \sum I_i}$

^c $R_{\text{pim}} = \frac{\sum \sqrt{1 - I_i}}{\sum I_i}$

^dCC_{1/2} = as defined by Karplus and Diederichs

^e $R_{\text{cryst}} = \frac{\sum |F_{\text{obs}} - F_{\text{calc}}|}{\sum F_{\text{obs}}}$, where F_{obs} and F_{calc} are the observed and calculated structure factors, respectively.

R_{free} is the same as R_{cryst}, but for 7.9% of the data randomly omitted from refinement.

Inhibition of enzyme activities

M^{Pro} activity testing. M^{Pro} activity was determined using BPS Bioscience assay kit according to vendor's manual. Mutant M^{Pro} were custom generated by BPS Biosciences with sequencing verification. For inhibitor potency against the mutants, M^{Pro} concentrations were adjusted based on mutant enzyme activities. The assay measures proteolytic cleavage of a fluoregenic M^{Pro} substrate over time. After substrate addition, kinetics of the reaction was measured at excitation/emission = 360/460 nm in a microplate reader (Tecan Spark) with data acquisition every 5 min for 1 h. The initial linear portion of the fluorescence change was selected for the analysis of M^{Pro} enzymatic activity in the absence and presence of inhibitors. % Activity is calculated as the initial rates of inhibitor treated samples divided by those of untreated samples. Dose-dependent inhibition and IC₅₀ analyses were performed using GraphPad Prism software.

Cathepsin activity testing. Activities of recombinant cathepsins L, S, B, F, and V were measured using respective fluorometric assay kits from BPS Bioscience and

the vendor protocols adapted to 384-well format. Cathepsin K assay kit was from BioVision. Substrate cleavage was measured every 5 min for 30–60 min at excitation/emission wavelengths = 360/440 nm for cathepsins L, S, B, F, and V. Cathepsin K activity was measured at excitation/emission wavelengths = 400/505 nm. Linear ranges of the kinetic curves were used to analyze dose-dependent inhibition of cathepsin activities by tested compounds. IC₅₀ values were determined using GraphPad Prism software.

In vitro antiviral assays

All experiments using live SARS-CoV-2 viruses were handled in BSL-3 laboratory.

Plaque reduction neutralization test. 18×10^3 Vero E6 cells were seeded per well in 96 well flat bottom plates and incubated overnight. Next day, medium was discarded and 50 μ L of compounds pre-diluted in media were transferred to Vero E6 cells. For plaque assay of Omicron samples, Vero E6-TMPRSS2-T2A-ACE2 in culture medium were used. After 2 h incubation, 1000 pfu/50 μ L of SARS-CoV-2 was added to each well and incubated for 1 h in 36°C 5% CO₂, followed by addition of 100 μ L of overlay (1:1 of 2% methylcellulose and culture medium) to each well. Plates were incubated for 3 days before crystal violet staining for plaques as described.⁵⁹ A reduction of plaques was calculated in relative to untreated wells.

Foci reduction neutralization test to determine in vitro antiviral activity. Confluent cells seeded in 96 well plate were grown overnight and pretreated with compounds for 2 h prior to infection with 500 pfu virus. One day after infection, cells were fixed and stained with 1:1000 anti SARS-CoV-2 NP, followed with 1:1000 Alexa Fluor 488 conjugated goat anti-mouse IgG as secondary antibody. Virus foci were counted using fluorescence microscope.

Released virus load in EpiAirway

EpiAirway were comprised of approximately 1.2×10^6 normal human bronchial epithelial cells differentiated at the air-liquid interface. Cells were grown on *trans*-well inserts placed in 12 well Holey top plates (HNG-TOP-12) with culture medium (AIR-100-MM) added to the basolateral side, and apical side exposed to a humidified 5% CO₂ environment at 37°C. On day 1, the culture medium in the basolateral side was replaced with freshly prepared media containing different concentrations of olgotrelvir. Two hours later, 100 μ L SARS-CoV-2 stock solutions were added to the apical side to infect EpiAirway at a multiplicity of infection (MOI) of approximately 0.1. After 1 h incubation, extra virus stock solutions were removed, and the apical side was washed with 400 μ L TEER buffer. Compound treatment at the basolateral side were refreshed every other day. After 3 and 5 days, viruses released into the apical compartment were harvested by the addition of 0.4 mL culture media, followed by the collection of the 0.4mL media after 30 min incubation. Viral titers were measured on Vero E6 cell.

Pseudovirus entry inhibition assay

Plasmids. All SARS-CoV-2 Spike constructs for pseudotype generation were expressed from plasmid pCDNA3.1 (ThermoFisher #V79020). Codon optimized SARS-CoV-2 Wuhan-1 Spike carrying the D614G amino acid change (Sino Biological #VG40589-UT (D614G)) was modified to remove the last 21 amino acids at the C-terminus (Spike Δ 21) and was used as the parental clone. Amino acid changes for each variant are as follows. Delta: T19R, G142D, Δ 156–157, R158G, L452R, T478K, D614G, P681R, and D950N. Omicron BA.1: A67V, del69–70, T95I, G142D, del143–145, N211D, del212, G339D, S371L, S373P, S375F, K417N, N440K,

G446S, S477N, T478K, E484A, Q493R, G496S, Q498R, N501Y, Y505H, T457K, D614G, H665Y, N679K, P681H, N764K, D796Y, N856K, Q954H, N969K, L981F. Omicron BA.4/5: V3G, T19I, L24S, del25-27, del69-70, G142D, V213G, G339D, S371F, S373P, S375F, T376A, D405N, R408S, K417N, N440K, L452R, S477N, T478K, E484A, F486V, Q498R, N501Y, Y505H, D614G, H665Y, N679K, P681H, N764K, D796Y, Q954H, N969K.

VSV-Spike pseudotype generation. To generate each Spike pseudotyped VSV, 1.2×10^6 BHK21 cells were nucleofected with 2 μg of Spike plasmid using an Amaxa Nucleofector II with cell line kit L (Lonza #VCA-1005) and program A-031. Cells were plated to one well of a 6-well dish and incubated overnight at $37^\circ\text{C}/5\%\text{CO}_2$. The next day, cells were transduced with G-Pseudotyped ΔG -luciferase ($\text{G}^*\Delta\text{G}$ -luciferase) rVSV (Kerafast #EH1025-PM) at $\text{MOI} \sim 4$ for 1 h at $37^\circ\text{C}/5\%\text{CO}_2$. Cells were rinsed twice with DPBS (Corning #21-031-CM), 2 mL of fresh media added, and incubated for 24–44 h at $37^\circ\text{C}/5\%\text{CO}_2$. Supernatants were collected, spun at 300g for 5 min at room temperature, aliquoted and stored at -80°C . Pseudotyped virus transduction was normalized for luciferase expression by incubating with 1 $\mu\text{g}/\text{mL}$ anti-VSV-G clone 8G5F11 (Millipore #MABF2337) for 30 min at room temperature followed by transduction of 293-ACE2 cells. $\text{G}^*\Delta\text{G}$ -luciferase VSV of known titer was used as the standard. Transduced cells were incubated for 24 h, 40 μL of ONE-Glo reagent (Promega #E6110) added and luminescence measured using a Tecan Spark plate reader.

Pseudotyped virus particle entry inhibition assays. Target cells were plated to white-walled 96-well plates at 40K cells/well and incubated at $37^\circ\text{C}/5\% \text{CO}_2$. The next day, cells were pretreated for 1 h with the noted compound or DMSO control. Pseudotyped VSV particles were incubated with anti-VSV-G (1 $\mu\text{g}/\text{mL}$) antibody for 30 min at room temperature and added to the target cells in triplicate. Transduced cells were incubated for 24 h, 40 μL of ONE-Glo reagent (Promega #E6110) added and luminescence measured using a Tecan Spark plate reader. Where noted, percent entry inhibition was calculated using $1 - ([\text{luminescence of treated sample}] / [\text{average luminescence of untreated samples}]) \times 100$.

In vivo antiviral testing

Olgotrelvir oral formulation. Olgotrelvir was formulated by dissolving in the vehicle solution (1.7% Poloxamer 124, 2.6% PEG-400, 2.8% Labrasol and 92.9% D5W [5% dextrose in water]). The oral dose was calculated based on 100 μL of drug solution each time for a 25-gram mouse. Therefore, for 1000 mg/kg, 25% w/w formulation (olgotrelvir/total mass) was prepared; for 500 mg/kg, 12.5% w/w formulation was prepared; for 400 mg/kg, 10% w/w formulation was prepared.

In vivo antiviral activity testing. 8–12 weeks old K18-hACE2 transgenic mice (weight range of 16.2–29.1 g) were infected intranasally with indicated pfu of SARS-CoV-2 in total volume 50 μL . Immediately after virus inoculation, or 12 h after, mice were orally administered with compounds in a volume of 100 μL twice a day. Body weights were recorded daily. At the end of the study, euthanasia was performed by CO_2 followed by thoracotomy. Collected BALF samples were run on Bio-Plex MAGPIX Multiplex Reader using Bio-Plex Pro Mouse Cytokine 23-plex Assay according to the manufacturer protocol. Lung tissues were collected from euthanized animals for virus titer determination and histopathology studies.

Determination of mice lung virus titer. The left lobe of sampled lungs was homogenized in a TissueLyser (Qiagen Inc., CA) operated at 25–30 Hz for 4 min. Clarified homogenate was serially diluted 10-fold to infect confluent monolayers of Vero E6

cells plated in 24 well plates. After 1h incubation, an overlay (1:1 of 2% methylcellulose and culture media) was added to each well and incubation commenced for 3 days at 36°C. Plaque staining was performed using Crystal Violet.

Histopathology study. After overnight fixation in 1 mL of PFA/Zinc, the collected lung tissues were sent to Histowiz (New York, NY) for embedding, cutting slides and staining. For pathology study, the slides were stained with Hematoxylin & Eosin (H&E), followed by an independent experienced veterinary pathologist consultation. Each lung sample was evaluated using a semi-quantitative analysis using four parameters: perivascular inflammation, bronchial or bronchiolar epithelial degeneration or necrosis, bronchial or bronchiolar inflammation, and alveolar inflammation. A 5-point scoring system for assessment of epithelial degeneration/necrosis and inflammation was utilized (0-with normal limits; 1-mild; scattered cell necrosis/vacuolation, few/scattered inflammatory cells, 2-moderate; multifocal vacuolation or sloughed/necrotic cells, thin layer of inflammatory cells, 3-marked; multifocal/segmental necrosis, epithelial loss/effacement, thick layer of inflammatory cells, 4-severe; coalescing areas of necrosis; parenchymal effacement, confluent areas of inflammation. A total pathology score was calculated for each mouse by adding the individual histopathological scores.

In situ evaluation of virus infection. To evaluate SARS-CoV-2 load and distribution in lung tissue, an immunohistochemical (IHC) staining with a Histowiz optimized antibody against SARS-CoV-2 nucleocapsid protein was used. The IHC were further analyzed using the Histowiz image analysis service with their automated quantitation program. Briefly, first, the most intensely stained slides were used to set thresholds to define intense positive staining (score = 3), medium positive staining (score = 2), light positive staining (score = 1), vs. what was designated as background (score = 0). Second, a computer program was used to obtain the area for each category of staining and % area was calculated as area/total tissue slice area. The total staining was represented by H-score, which was calculated as: $1 \times (\% \text{ area-low}) + 2 \times (\% \text{ area-medium}) + 3 \times (\% \text{ area-high})$.

Generation of CTSL KO cell line

CRISPR/Cas9-mediated CTSL KO in HEK Blue-hACE2-TMPRSS2 cell was generated by Synthego (Redwood City, CA, USA). Briefly, a ribonucleoprotein (RNP) complex consisting of purified Cas9 nuclease and a gene-specific synthetic guide RNA (gRNA, sequence: UAGAGGCACAGUGGACCAAG) was delivered into the cells by electroporation. Mock-transfected (non-edited) cells were generated in parallel. Knockout efficiency in CRISPR-edited cell pool was ~90% as demonstrated by Sanger sequencing and Interference of CRISPR Edits (ICE) analysis-based QC report (provided by Synthego). Sequences of PCR primers are: FOR primer (5'-3'): GCCTCTCCACAGTCCTTGG; REV primer (5'-3'): TGTGCTCATAATCCACGCCA. The sequencing primer sequence is: ATAATCCACGCCATTAGGTTATTACATTAG. Before using the cells for pseudotype entry testing, the efficiency of CTSL KO was further verified by Western Blot analysis. Cleared cell lysates (15–20 µg) from KO and parental cells were resolved by SDS page; CTSL was detected using mouse anti-human CTSL antibody (Invitrogen, BMS1032; dilution 1:1000), followed by HRP conjugated anti-mouse IgG (Cell Signaling, 7076; dilution 1:2000). Anti-actin (Sino Biological, 100166-MM10; dilution 1:1500) was used as a loading control.

Cytotoxicity testing

For cell panel cytotoxicity evaluation, cells were seeded and incubated overnight to reach log phase growth the next day. To evaluate potential mitochondrial toxicity,

cells were plated in DMEM culture media containing 10 mM galactose or 25 mM glucose. To calculate selective index, in parallel with antiviral activity testing, the same cells were seeded in a separate set of 96 well plates at the same density so that they were confluent the second day. Compound treatment was initiated the next day and treated cells were incubated for 3 additional days. Cell viability was measured using CellTiter-Glo reagent (Promega); luminescence was measured in Tecan Spark microplate reader. Data were calculated as percentages of the signal from wells with untreated cells under the same growth condition.

Protease panel inhibition testing

AC1115 inhibition of a diverse protease panel was conducted by BPS Biosciences. Briefly, activities of recombinant proteases were determined using *in vitro* TR-FRET assays available as BPS commercial kits. 1 μ M AC1115 were tested for inhibition of human proteases, 100 nM AC1115 were tested for inhibition of virus proteases. Reference inhibitors for each protease were tested at three concentrations (0.1x, 1x and 10x IC_{50} values) as internal control. All tests were conducted in duplicates, with a final DMSO concentration of 1% in the reaction mixture. The fluorescent intensity in the absence of compound (Ft) in each dataset was defined as 100% activity. The fluorescent intensity in the absence of the enzyme (Fb) in each dataset was defined as 0% activity. The percent activity in the presence of each compound was calculated according to the following equation: % activity = (F-Fb)/(Ft-Fb), where F = the fluorescent intensity in the presence of the compound.

AC1115 SAFETYscan47 KdMAX Panel Screening

The SAFETYscan47 KdMAX Panel Screening was conducted by Eurofins DiscoverX Corporation (San Diego, CA). The panel includes targets and pathways which are now well established as contributors to clinical ADRs. Total 78 assays were conducted against 47 targets. For each assay, AC1115 was tested in 10 doses, from 100 μ M to 3.3 nM with half log dilution. The assays performed include: cAMP assays utilizing the PathHunter enzyme fragment complementation technology; NHR (nuclear hormone receptor) nuclear translocation determination; FLIPR-based cellular screening assays for calcium flux and ion channel assays; KINOMEScan kinase binding assays; and a variety of enzymatic activity assays. For each assay, reference compounds were tested together with AC1115 as controls. For data analysis, response was capped at 0% or 100%, where calculated percent response returned a negative value or a value greater than 100, respectively. IC_{50}/EC_{50} were calculated based on dose dependent percentage of responses.

Metabolic stability study

Test compound (0.2 μ M) was incubated in human liver microsome (HLM) (1.0 mg/mL) diluted in potassium phosphate buffer (100 mM, pH 7.4) supplemented with 2 mM $MgCl_2$ and 1.3 mM NADPH. At various time points, samples were quenched by protein precipitation, followed by LC-MS/MS analysis. Substrate depletion half-life ($t_{1/2}$), intrinsic clearance (CL_{int}) and Extraction ratio (ER) were calculated.

Cytochrome P450 reaction phenotyping

P450 enzymes involved in the metabolism of AC1115 were identified by the use of selective inhibitors, and *in vitro* studies using microsomal fractions from cells expressing individual P450 enzymes.

Chemical inhibition method. Incubations were conducted in 100 mM potassium phosphate buffer (pH 7.4) containing 1 mM NADPH, 0.5 mg/mL HLM, and 1 μ M AC1115 at 37°C for 0–60 min in the absence or presence of selective the specific

inhibitors of CYP1A2, CYP2B6, CYP2C8, CYP2C9, CYP2C19, CYP2D6 and CYP3A4. Same tests were also conducted in the absence of NADPH. Reactions were quenched by protein precipitation, followed by LC-MS/MS analysis. Remaining of parent compound and metabolic contribution of CYP450 isozymes were calculated.

Recombinant enzyme method. Incubations were conducted in 100 mM potassium phosphate buffer (pH 7.4) containing 2 mM NADPH, 1 μ M AC1115, and recombinant enzymes at different concentrations (CYP1A2 (266.7 nM), CYP2B6 (333.3 nM), CYP2C8 (333.3 nM), CYP2C9 (133.3 nM), CYP2C19 (466.7 nM), CYP2D6 (66.7 nM) and CYP3A4 (133.3 nM)). After 37°C for 0–60 min, reactions were quenched by protein precipitation, followed by LC-MS/MS analysis. The residual rate (%Remaining) at the appointed time point, clearance rate (CL_{int}) and contribution (Contribution_x) of each CYP450 isozyme in human liver microsomes were calculated.

CYP inhibition

The potential of AC1115 to inhibit the activity of the major human P450 enzymes (CYP1A, CYP2B6, CYP2C8, CYP2C9, CYP2C19, CYP2D6 and CYP3A4) was studied in human hepatic microsomes *in vitro*.

Cytochrome P450 (CYP) inhibition assay (IC_{50}). Isoform-specific substrates were incubated individually with human liver microsomes and a range of test compound concentrations (0.137–100 μ M) for the specified time. Reactions were quenched by protein precipitation, followed by LC-MS/MS analysis. The relative activity of CYP450 (% of negative control) and IC_{50} value were calculated.

Cytochrome P450 time dependent inhibition (IC_{50} shift) assay. The IC_{50} shift assay determines the IC_{50} value (concentration which produces 50% inhibition) of test compound under three different experimental conditions; 0 min pre-incubation, 30 min pre-incubation minus NADPH and 30 min pre-incubation plus NADPH. Following the pre-incubation, isoform-specific substrates are added to measure the residual enzyme activities. If the compound is a time-dependent inhibitor a shift to the left (increase in potency) will occur between the 30 min pre-incubation minus NADPH and 30 min pre-incubation plus NADPH. The ratio of these two values gives the IC_{50} shift.

Transporter (BCRP) inhibition

The inhibitory potential of olgotrelvir and AC1115 on ATP-binding cassettes (ABC) BCRP and MDR1 transporter was evaluated using vesicle membrane expressing the above transporters.

Samples with ATP: 10 μ L dosing solutions of the test article or negative control was pre-incubated with 10 μ L of 5 mg/mL vesicles and 5 μ L of reaction buffer at 37°C water bath for 5 min; 20 μ L of 10 mM ATP solution and 5 μ L probe substrate (N-methylquinidine (NMQ) for P-gp, Lucifer yellow for BCRP) working solution were pre-incubated at 37°C for 5 min. The two solutions were then combined and incubated at 37°C for an additional 5 min. After incubation, the pre-cooled quenching & washing buffer solution was added into the incubation system to terminate the transporter reaction. Samples were then transferred to a 96-well filter plate. After washing the filter 5 times with 0.2 mL of pre-cooled quenching and washing buffer, the vesicles on the filter were dissolved using 50 μ L 10% SDS. The filtrate was collected after centrifugation at 2000 rpm for 2 min. The procedure of dissolving and centrifugation was repeated once. Two filtrates were combined and mixed with an equal volume of

0.1 N H₂SO₄ (for P-gp) or DMSO (BCRP). The amount of NMQ or Lucifer yellow was determined by Microplate Reader.

Evaluation of AC1115 as a potential substrate of BCRP and MDR1

Membrane vesicles expressing ABC transporters MDR1 and BCRP were used to evaluate whether the test article (AC1115) was a substrate. The test concentrations of test article were 1, 10 and 50 μM.

Samples with ATP: In the test group, 10 μL working solution of the test article and 5 μL of reaction buffer or working solution of inhibitors (Novobiocin for BCRP, Cyclosporine A for MDR1) were pre-incubated with 20 μL 10 mM ATP solution at 37°C for 5 min as mixture A. In the positive control (PC) group, 10 μL probe substrates (Lucifer yellow for BCRP and NMQ for MDR1) and 5 μL reaction buffer or working solution of inhibitors were pre-incubated with 20 μL 10 mM ATP solution at 37°C for 5 min as mixture B. At the same time 10 μL vesicles and 5 μL 10 mM ATP solution were pre-incubated as mixture C. After pre-incubation, in the test group, the mixture A was incubated with the mixture C at 37°C for an additional 5 min; in the PC group, the mixture B was incubated with the mixture C at 37°C for an additional 5 min. The total incubation volume was 50 μL. To prepare samples with AMP, 10 mM AMP solution was used instead of 10 mM ATP solution as described above. After incubation, the pre-cooled quenching & washing buffer solution was added into the incubation system to terminate the transporter reaction. Samples were then transferred to a 96-well filter plate. Washed and dissolved the vesicles, then the filtrate was collected. The content of test article was determined by LC-MS/MS, and the amount of Lucifer yellow (BCRP) or NMQ (MDR1) was determined by Microplate Reader.

Pharmacokinetics

Mouse and Rat pharmacokinetics (PK) studies, as well as bioanalysis of dog plasma samples were performed at Hangzhou ACEA Pharmaceutical Research Co., Ltd. Dog PK studies were conducted at Medicilon Preclinical Research (Shanghai) LLC. The composition of each oral galvage (PO) dosing vehicle is as below: 1.7% (Poloxamer 124) + 2.6% PEG400 + 2.8% (Labrasol ALF) + 92.9% D5W (5% Glucose Injection) = w: w: w; for IV (vehicle 2): 25% PEG400 + 75% D5W.

Balb/c mice and SD Rats were purchased from Vital River (Zhejiang, China) and were typically 7–10 weeks of age at the time of dosing; Beagle dogs were purchased from Shen Yang Kang Ping Institute of Laboratory Animals (China), subjects 7 to 8 months of age were used in studies. During the studies, water was provided *ad libitum*. Animals were fasted overnight, fed 4 h post-dose for single dose, and provided food during the study for 7-day repeated dose. Olgotrelvir was administered intravenously (IV) via the tail vein with doses of 10 mg/5 mL/kg to mice, 5 mg/2 mL/kg to rats and 2 mg/1 mL/kg to dogs. In separate experiments, olgotrelvir was administered via oral gavage (PO) at doses of (300, 500 and 1000 mg/kg, 10 mL/kg) to mice, (100, 200 and 500 mg/kg, 10 mL/kg) to rats and (12.5, 25 and 50 mg/kg, 10 mL/kg) to dogs, respectively. At predetermined time points after dosing, blood samples were collected via the orbital sinus vein or jugular vein into tubes containing K₂-EDTA and stored on wet ice until centrifugation to obtain plasma, which was stored frozen at –80°C.

In order to investigate the effect of RTV (a CYP3A4 inhibitor) on the absorption of olgotrelvir, RTV was administered twice daily at 12.5 mg/kg/dose or 16 mg/kg/dose for

consecutive 13 doses to mice before a single dose of AC1115 (IV, 10 mg/kg) or olgotrelvir (PO, 40 mg/kg).

General toxicity studies

Study designs and parameters evaluated in toxicology studies were consistent with accepted principles and practices as outlined in ICH and national regulations (US FDA and China FDA). All definitive studies were conducted in accordance with US and China FDA GLP regulations.

Repeat dose toxicity studies with olgotrelvir

Briefly, groups of male and female Sprague-Dawley (SD) rats or beagle dogs were administered vehicle [1.7% (w/w) Poloxamer 124, 2.6% (w/w) PEG 400, 2.8% (w/w) Labrasol ALF, and 92.9% (w/w) D5W] or different doses of olgotrelvir in vehicle as listed in [Data S19](#). Study evaluations included detailed clinical observations, body weights, food consumption, micronucleus assessment (rat only), electrocardiography (dogs only), ophthalmology, clinical pathology (hematology, clinical chemistry, coagulation, urinalysis), toxicokinetics, gross and microscopic pathology. Adversity assessments and considerations for setting the no-observed-adverse-effect-levels included integrated evaluation of the incidence and severity of clinical and pathology findings.

Safety pharmacology studies with olgotrelvir

A program of GLP-compliant studies representing the Core Battery of safety pharmacology studies described in the International Conference on Harmonization (ICH) S7A and S7B Tripartite Guideline was conducted.

For central nervous system study, fifty SD rats were assigned to five groups (5/sex/group) and administered with 500, 1000, or 2000 mg/kg olgotrelvir and vehicle control article via oral gavage. The dose volume was 20 mL/kg. Administration of 15 mg/kg chlorpromazine HCl injection was used as positive control group. The dose volume was 10 mL/kg. The functional observational battery (FOB) test, forelimb grip strength and body temperature measurement (rectal temperature) were performed pre-dose (0 h) and at 10 min, 1 h, 4 h, 6 h, and 24 h post-dose.

For cardiovascular study in conscious telemetered beagle dogs, a total of 8 beagle dogs (4 males and 4 females) implanted with telemetric transmitters for ECG measurements and blood pressure received a single oral gavage of olgotrelvir at 0, 50, 100, or 200 mg/kg with a dose volume of 5 mL/kg. A 4 × 4 Latin Square design of this study was applied for males and females with at least 20 h washout period between each treatment. Clinical signs were monitored twice daily on dosing days (before and after dosing) and once daily on washout days. Body weight was recorded for all animals prior to randomization, which was used for randomization and dose amount calculation, respectively. Parameters such as mean blood pressure (MBP), systolic blood pressure (SBP), diastolic blood pressure (DBP), PR interval (PR), QRS duration (QRS), RR interval (RR), QT interval (QT), heart rate (HR) and heart rate corrected QT interval (QT_{cv}) were measured at pre-dose (2 timepoints pre-dosing with an interval of at least 30min), 0.5 h, 1 h, 2 h, 6 h and 24 h post dosing by using Noninvasive Telemetry Animals Physiological Data System EMKA Technologies Inc. Heart rate corrected QT interval (QT_{cv}) and percentage of changes of each parameters were also calculated.

For hERG study, AC1115 was evaluated on HEK293 cells transfected hERG potassium channels. Cells were treated with extracellular solution containing 0.3%

DMSO (negative control), and AC1115 at 30, 60, 90 and 120 $\mu\text{mol/L}$. In addition, different cells were treated with cisapride at 0.06 and 0.21 $\mu\text{mol/L}$ (positive control). The hERG currents were continuously recorded at room temperature and protected from light, using the whole-cell patch-clamp method. The percentage of current inhibition was calculated following the test of control article treatments.

In vivo micronucleus assessment in rats

The potential of olgotrelvir to induce chromosome damage was determined by the increased frequency of micronucleated reticulocytes in peripheral blood samples from vehicle- and olgotrelvir-treated rats from the 2-week GLP toxicity study. The micronucleus portion of this study was designed using ICH Harmonised Tripartite Guideline M3 (R2) and Guiding Principles of Drug Study on Genetic toxicity of technology by China FDA. Briefly, 5 rats/group per sex were used for micronucleus analysis. The blood samples were collected on D15. After that, the blood samples were fixed, stored at long term services and supports facilities, before analyzed by flow cytometry for micronucleus evaluation. Approximately 20000 reticulocytes (RET) were analyzed for each animal to determine the frequency of micronucleated reticulocytes (%MN-RET) and the percentage of reticulocytes in total erythrocytes (%RET).

Bacterial reverse mutation assay with olgotrelvir

The mutagenic potential of olgotrelvir was evaluated on inducing reverse gene mutations at the histidine locus in five strains of *Salmonella typhimurium* (TA97a, TA98, TA100, TA102, and TA1535). 50 mg/mL (5000 $\mu\text{g/plate}$) was selected as the highest concentration in this study. The final concentrations used in this study were set as 156, 313, 625, 1250, 2500, and 5000 $\mu\text{g/plate}$ with or without S9 metabolic activation.

The standard plate incorporation method was used in the study in the presence or absence of S9 metabolic activation system. Three plates were cultivated in parallel for each treatment condition. The plates were incubated for 48 to 72 h at $37 \pm 2^\circ\text{C}$, and then the number of revertant colonies on each plate was counted.

In vitro chromosome aberration test of olgotrelvir in Chinese hamster lung cells

The clastogenic potential of olgotrelvir was evaluated on inducing structural chromosome aberrations in cultured CHL cells. The concentrations selected for the test article in the *in vitro* chromosome aberration test were 125, 250 and 500 $\mu\text{g/mL}$ under the 4h + S9 treatment conditions and 24hr-S9 treatment condition. The chromosome aberration test was conducted with and without metabolic activation (+S9/-S9). Under the 4h + S9 treatment conditions, cells were treated with the test article, negative or positive controls for about 4 h with or without S9, followed by removal of the treatment medium and the cells were then cultured for approximately 20 additional hours in the growth medium. Under the 24hr-S9 treatment conditions, cells were treated with the test article, negative control, or positive control for approximately 24 h without S9. These cells were harvested and the slides were prepared after cells were treated with hypotonic solution, fixed, dropped on slides, stained in Giemsa, and mounted. The slides were evaluated with blinded codes under an oil immersion objective. For each treatment, 300 metaphase cells were evaluated for chromosomal aberrations (Only 100 metaphase cells were evaluated when the frequency of aberrant cells was >20%). The types and numbers of structural and numerical aberrations were recorded.

First-in-human clinical trial

FIH Study MPR-COV-101AU, "A Randomized, Double-Blind, Placebo-Controlled, Phase I Study to Assess the Safety, Tolerability, and Pharmacokinetics of Single

and Multiple Oral Doses of Olgotrelvir in Healthy Volunteers,” was a two-part SAD/MAD study. In Part 1, healthy adult subjects received a single oral dose of 300 mg, 600 mg, 1200 mg or 2000 mg with 240 mL water after an overnight fast. Subjects within a cohort was randomized to a single dose of either olgotrelvir or placebo in a 3:1 or 4:1 ratio. From the perspective of safety, sentinel dosing was used in each cohort (except for the Period 2 study), and the first 2 subjects in each cohort were randomized 1:1 to olgotrelvir or placebo. After the Investigator had reviewed the first 24 h of safety data for the first 2 subjects in a cohort, the remaining subjects in the cohort were randomized 5:1 or 7:1 to olgotrelvir or placebo. In Part 2, repeated oral doses twice daily (BID) were administered for 7.5 days (15 doses) at 300 mg, 600 mg and 800 mg with 8 subjects in each cohort. Subjects within a cohort were randomized to either olgotrelvir or placebo in a 3:1 ratio and received the study drug every 12 h for 7 days, with a single dose administered on the morning of Day 8 for collection of PK samples. The study was conducted at a Phase 1 unit in Sydney (Randwick), Australia (Scientia Clinical Research Limited). The protocol (Method S1) was approved by Bellberry human research ethics committee of Australia (Application No: 2022-04-380-A-3). This study was conducted in compliance with the clinical study protocol (and amendments), International Council for Harmonisation of Technical Requirements for Pharmaceuticals for Human Use, Good Clinical Practice, and applicable regulatory requirements.

The number of subjects (planned and analyzed) in different study populations was listed below.

Number of Subjects	Total		Part 1 (SAD)		Part 2 (MAD)	
	active	placebo	active	placebo	active	placebo
Planned	44	14	26	8	18	6
Screened	122		71		51	
Screening failure	61		35		26	
Randomized	61		36		25	
treated	44	16	26	8	18	6
Early withdrawals/discontinuations	3	0	2	0	1	0
Full Analysis set (FAS)	61		36		25	
Safety Analysis Set (SS)	58		34		24	
PK Concentration analysis set (PKCS)	44		26		18	
PK Parameter Analysis Set (PKPS)	44		26		18	

FAS: All randomized subjects receiving at least one dose of OLGOTRELVIR and had at least one evaluable pharmacokinetic parameter without any major protocol deviations/violations that have obvious effects on pharmacokinetic parameters.

SS: All subjects who receive at least one dose of study drug.

PKCS: All randomized subjects receiving at least one dose of OLGOTRELVIR and had at least one evaluable plasma/urine drug concentration after dosing.

PKPS: All randomized subjects receiving at least one dose of OLGOTRELVIR and had at least one evaluable pharmacokinetic parameter without any major protocol deviations/violations that have obvious effects on pharmacokinetic parameters.

Pharmacokinetic assessment. Plasma samples for pharmacokinetic assessments, were collected up to 72 h post dose and were analyzed for AC1115 concentration at Agilix Biolab, Australia, using a validated sensitive and specific LC-MS/MS

method in compliance with FDA and EMA guidelines on Bioanalytical Method Validation and OECD Series on Principles of Good Laboratory Practice.

Pharmacokinetic analysis. The main PK parameters including but not limited to C_{max} , T_{max} , AUC_{0-tr} , AUC_{inf} , CL , V_{ss} , MRT_{0-tr} , CL/F and Vz/F , were estimated using noncompartmental analysis (Phoenix WinNonlin 8.3). Detailed statistical analysis was described in Method S2.

Safety assessment. All safety analyses were performed based on the SS. Safety was assessed on the basis of AEs, clinical laboratory data, vital signs, 12-lead ECG parameters, and PEs. Safety analysis involved examination of the descriptive statistics and individual patient listings for any effect of study treatment on safety. AEs were coded and classified according to the MedDRA (Version 25.0) with System Organ Class (SOC) and Preferred Term (PT).

Phase I clinical trial in COVID-19 patients

MPR-COV-101CN study “A Randomized, Double-Blind, Placebo-Controlled Phase I Clinical Study Evaluating the Safety of a Single Ascending Dose of STI-1558 in Healthy Subjects and the Safety, Pharmacokinetics, and Efficacy of Multiple Ascending Doses of STI-1558 in SARS-CoV-2-Positive Subjects”, was a two-part SAD/MAD study. In Part 1 (SAD), healthy Chinese adult subjects received a single oral dose of 300 mg, 600 mg, 1200 mg or 2000 mg with 240 mL water after an overnight fast.

In Part 2, MAD study was conducted in SARS-CoV-2 positive asymptomatic and mild adult subjects. The study drug was scheduled to be administered orally once every 12h \pm 1 h (q12h \pm 1h). Subjects fast for at least 8 h before the first dose in every morning, 1 h after the administration, and fast for 1 h before and after the second dose, with 240 mL (about 300mL allowed for subjects in the 600mg and 800mg BID cohorts) of water. All subjects take their drugs within 5 min. Dose D1 to D7, q12h, once in the morning of D8 for a total of 15 doses. Subjects were followed up on D10, D14, D21, and D29 for safety and efficacy tests. The study was conducted at a Phase 1 unit at The Third People’s Hospital of Shenzhen in China.

The protocol (Method S3) was approved by China National Medical Product Administration (NMPA) (Application No: CXHL2200534) This study (NCT05523739) was conducted in compliance with the clinical study protocol (and amendments), International Council for Harmonisation of Technical Requirements for Pharmaceuticals for Human Use, Good Clinical Practice, and applicable regulatory requirements.

The number of subjects in different study populations was listed below.

Number of Subjects	Part 1 (SAD)		Part 2 (MAD)	
	active	placebo	active	placebo
Screened	115		62	
Screening failure	83		15	
Randomized	32		47	
treated	24	8	33	13
Early withdrawals/discontinuations	0	0	3	0
Full Analysis set (FAS)	32		46	
Safety Analysis Set (SS)	32		46	
PK Concentration analysis set (PKCS)	24		19	
PK Parameter Analysis Set (PKPS)	24		19	
modified intention-to-treat (mITT)			41	

Safety assessment. The analysis was conducted on the safety set (SS).

Adverse events and adverse reactions. All adverse events were coded using MedDRA (Version 25.0).

The overall situation of adverse events was summarized by the treatment cohort, and the overall incidence of various adverse events was calculated: adverse events, treatment-emergent adverse events, adverse drug reactions, serious adverse events, adverse events leading to early withdrawal, and adverse events leading to death.

Among treatment-emergent adverse events, treatment-emergent adverse events and adverse drug reactions were calculated by the system organ class (SOC) and the preferred term (PT), if a subject experienced the adverse event under the same SOC and PT many times, only one was counted under this SOC and PT.

Among treatment-emergent adverse events, the incidence of treatment-emergent adverse events and adverse drug reactions was calculated by SOC, PT and severity. If a subject experienced the adverse event under the same SOC and PT many times, only one with the worst severity was counted under this PT.

Laboratory tests. The laboratory hematology, urinalysis, blood chemistry, and coagulation function results of each visit from the baseline were statistically described by the treatment cohort.

The normal and abnormal changes of each variable before and after administration were compared through the shift table of clinical judgment before and after administration.

Vital signs. The vital sign results of each visit from the baseline were statistically described by the treatment cohort, and the normal and abnormal changes of each test value before and after administration was compared through the shift table of clinical judgment before and after administration (if applicable).

Physical examination. The normal and abnormal changes in each cohort before and after administration were compared through the shift table of clinical judgment before and after administration.

12-Lead ECG. From the baseline, the heart rate, QT, QTcF, QRS, and PR interval test results of each visit were statistically described. The normal and abnormal changes in each cohort before and after administration were compared through the shift table of clinical judgment before and after administration.

Pharmacokinetic analysis

Plasma concentration analysis. During the study, PK samples were collected from the subjects at the time points planned in the protocol for PK analysis. Based on PKCS, the plasma concentrations of AC1115 of subjects at various planned sampling time points were present using descriptive statistics by the study period, cohort and administration cycle. The subjects whose PK sampling time deviates from the time window specified in the protocol were tabulated.

PK parameter analysis. The non-compartmental analysis (NCA) of WinNonlin 8.3.1 was used to calculate the PK parameters according to the actual sampling time points.

Based on PKS, the PK parameters of AC1115 of subjects were tabulated and presented using descriptive statistics by the study period, cohort and administration cycle.

Efficacy analysis (for MAD study only)

Quantitative levels of SARS-CoV-2 RNA. Efficacy analyses were performed on the modified intention-to-treat set. SARS-CoV-2 RNA copy number from study subject nasal swab samples was determined by Guangzhou Daan Gene.

From the baseline, the quantitative level of SARS-CoV-2 RNA at each visit and the change from the baseline were statistically analyzed by the treatment cohort. The difference in change compared with the placebo cohort was tested using the t test, and the average value of the N genotype was summarized.

The number and percentage of subjects whose RNA quantitative level was lower than the lower limit of detection at each visit point were calculated, and Fisher's exact method was used for comparison between cohorts. Referring to the Diagnosis and Treatment Protocol for Novel Coronavirus Pneumonia (Version 9), the RNA quantitative level lower than the lower limit of detection is defined as a CT value greater than 35.

QUANTIFICATION AND STATISTICAL ANALYSIS

Statistics significance was evaluated in GraphPad Prism, using unpaired, two-tailed t test or two-way ANOVA. For clinical data, SAS version 9.4 was used for statistical analysis and graphing. In general, descriptive statistics, including the number of cases (n), arithmetic mean (Mean), standard deviation (std), median (Median), minimum (Min) and maximum (Max) values, were presented for the measurement data. For some measurement data, coefficient of variation (%CV), geometric mean (GeoMean), lower quartile (Q1), upper quartile (Q3), geometric standard deviation (GeoSD) and geometric coefficient of variation (%CVb) were also presented. For the enumeration data, the number of cases (n) and the percentage (%) were generally presented. Detailed description for statistical analysis of clinical data were included in [Methods S2](#) and [S4](#).